Accepted Manuscript

Submission Date: 2021-01-26
Accepted Date: 2021-03-18
Publication Date: 2021-04-01

Organic Materials

Synthesis and Self-Assembly Behavior of Double Ullazine-Based Polycyclic Aromatic Hydrocarbons

Marcus Richter, Michał Borkowski, Yubin Fu, Evgenia Dmitrieva, Alexey A Popov, Ji Ma, Tomasz Marszalek, Wojciech Pisula, Xinliang Feng.

Affiliations below.

DOI: 10.1055/a-1472-6852

Please cite this article as: Richter M, Borkowski M, Fu Y et al. Synthesis and Self-Assembly Behavior of Double Ullazine-Based Polycyclic Aromatic Hydrocarbons. Organic Materials 2021. doi: 10.1055/a-1472-6852

Conflict of Interest: The authors declare that they have no conflict of interest.

Abstract:
Polycyclic aromatic azomethine ylides (PAMY, 1) are versatile building blocks for the bottom-up synthesis of nitrogen-containing polycyclic aromatic hydrocarbons (N-PAHs). Although the chemistry of PAMY was already established few years ago, the cycloaddition of a double PAMY building block has not been reported so far. In this work, we demonstrate the first cycloaddition of a PAMY-dimer (6), which opens the access to three different alkyl ester-substituted N-PAHs with a laterally extended double ullazine scaffold (DU-1, DU-2 and DU-3). Interestingly, the cyclic voltammetry of DU-1-3 exhibited three reversible oxidation waves, which confirmed the electron-rich nature of the double ullazine scaffold. Furthermore, in-situ spectroelectrochemistry study of ethylhexyl ester-substituted DU-3 revealed the formation of different cationic species with new absorption bands up to 1689 nm. Additionally, the influence of the attached substituents on the film formation and supramolecular organization in the thin films were investigated by polarized optical microscopy and grazing incidence wide-angle X-ray scattering.

Corresponding Author:
Xinliang Feng, TU Dresden, Faculty of Chemistry and Food Chemistry, Dresden, Germany, xinliang.feng@tu-dresden.de

Affiliations:
Marcus Richter, TU Dresden, Faculty of Chemistry and Food Chemistry, Dresden, Germany
Michał Borkowski, Lodz University of Technology, Department of Molecular Physics, Lodz, Poland
Yubin Fu, TU Dresden, Faculty of Chemistry and Food Chemistry, Dresden, Germany
[...]
Xinliang Feng, TU Dresden, Faculty of Chemistry and Food Chemistry, Dresden, Germany

Synthesis and Self-Assembly Behavior of Double Ullazine-Based Polycyclic Aromatic Hydrocarbons

Marcus Richter[a] (ORCID: 0000-0003-0316-1160)
Michal Borkowski[b] (ORCID: 0000-0003-3440-8592)
Yubin Fu[a] (ORCID: 0000-0002-2613-394X)
Evgenia Dmitrieva[c] (ORCID: 0000-0001-7490-617X)
Alexey Popov[c] (ORCID: 0000-0002-7596-0378)
Ji Ma[a] (ORCID: 0000-0003-4418-2339)
Tomasz Marszalek[b,d] (ORCID: 0000-0003-3322-0766)
Wojciech Pisula[b,d] (ORCID: 0000-0002-5853-1889)
Xinliang Feng*[a] (ORCID: 0000-0003-3885-2703)

[a] Chair for Molecular Functional Materials, Center for Advancing Electronics Dresden (cfaed), Faculty of Food Chemistry and Chemistry, Technische Universität Dresden, Mommsenstraße 4, 01069 Dresden, Germany. xinliang.feng@tu-dresden.de

[b] Department of Molecular Physics, Faculty of Chemistry, Lodz University of Technology, Zeromskiego 116, 90-924 Lodz, Poland.

[c] Center of Spectroelectrochemistry, Nanoscale chemistry, Leibniz Institute for Solid State and Materials Research (IFW), Helmholtzstrasse 20, 01069 Dresden, Germany.

[d] Max Planck Institute for Polymer Research, Ackermannweg 10, 55128, Mainz, Germany.

Dedicated to Professor Peter Bäuerle on the occasion of his 65th birthday

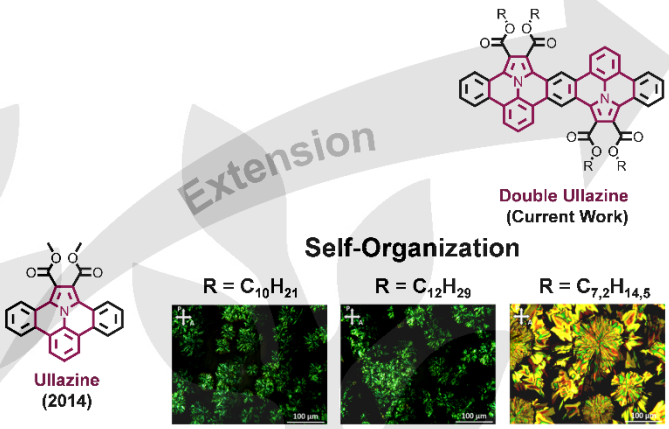

Received:
Accepted:
Published online:
DOI:

Abstract Polycyclic aromatic azomethine ylides (PAMY, **1**) are versatile building blocks for the bottom-up synthesis of nitrogen-containing polycyclic aromatic hydrocarbons (*N*-PAHs). Although the chemistry of PAMY was already established few years ago, the cycloaddition of a double PAMY building block has not been reported so far. In this work, we demonstrate the first cycloaddition of a PAMY-dimer (**6**), which opens the access to three different alkyl ester-substituted *N*-PAHs with a laterally extended double ullazine scaffold (**DU-1**, **DU-2** and **DU-3**). Interestingly, the cyclic voltammetry of **DU-1-3** exhibited three reversible oxidation waves, which confirmed the electron-rich nature of the double ullazine scaffold. Furthermore, *in-situ* spectroelectrochemistry study of ethylhexyl ester-substituted **DU-3** revealed the formation of different cationic species with new absorption bands up to 1689 nm. Additionally, the influence of the attached substituents on the film formation and supramolecular organization in the thin films were investigated by polarized optical microscopy and grazing incidence wide-angle X-ray scattering.

Key words polycyclic aromatic hydrocarbons, nanographenes, polycyclic aromatic azomethine ylides, cycloaddition, ullazine

Introduction

Polycyclic aromatic hydrocarbons (PAHs), which can be considered as small cutouts of graphene, are a remarkable class of organic compounds with unique (opto)electronic properties.[1] A continuous advancement in the reaction methodology and molecular design for the development of functionalized PAHs was devoted in order to tune their (opto)electronic properties and to enable an implementation into organic electronics.[2] One efficient pathway to tailor the intrinsic optical and electronic properties of PAHs is the introduction of nitrogen atoms, which may lead to control over the energy level of the frontier orbital or the stabilization of charges and radicals.[3] For example, the nitrogen-containing PAHs with an 16 π-electron ullazine motif have evolved as an attractive class of PAHs for dye-sensitized solar cells.[4] Although the first ullazine derivatives were already reported by Zeller in 1983,[5] the synthesis of ullazine-embedded PAHs still remains challenging and is mostly limited to acid-promoted and metal-catalyzed cyclization reactions.[6]

In 2014, our group firstly reported the synthesis of polycyclic aromatic azomethine ylides (PAMYs, **1**), which are unique building blocks for the construction of unprecedented nitrogen-containing PAHs (*N*-PAHs) *via* radical or zwitterionic pathway (Figure 1a).[7] Especially, the 1,3-dipolar cycloaddition between PAMY (**1**) and alkenes/alkynes (**2**) with subsequent dehydrogenation is a powerful tool for the formation of ullazine-based PAHs (**3**).[8] Moreover, the 1,3-dipolar cycloaddition with PAMY (**1**) was recently extended to the use of nitriles (**4**) as dipolarophiles and allowed the formation of azaullazine derivatives (**5**) on surface as well as in solution.[9] While the cycloaddition of the PAMY building block (**1**) has already been intensively investigated in the last few years, the 1,3-dipolar cycloaddition of an extended PAMY dimer is not known so far.

In this work, we demonstrate the first cycloaddition of PAMY-dimer (**6**), which allows the synthesis of three novel alkyl ester-substituted *N*-PAHs with a laterally extended double ullazine scaffold (**DU-1**, **DU-2** and **DU-3**, Figure 1b). The optoelectronic properties of **DU-1-3** are comprehensively investigated by UV-Vis absorption spectroscopy, fluorescence spectroscopy, and cyclic voltammetry (CV) as well as supported by theoretical modelling *via* density functional theory (DFT) calculations. In particular, the cyclic voltammetry of **DU-1-3** showed three reversible oxidations waves, which confirmed the electron-rich structure of the double-ullazine framework. Moreover,

spectroelectrochemistry (SEC) measurements unraveled several cationic species for **DU-3**, which were verified by UV-Vis-NIR absorption and electron paramagnetic resonance (EPR) spectroscopies. Furthermore, the self-organization of **DU-1-3** was investigated by polarized optical microscopy (POM) and grazing-incidence-wide-angle-X-ray-scattering (GIWAXS) measurements. In contrast to linear alkyl ester-substituted **DU-1** and **DU-2** (*C_{10} to C_{12}*), the assemblies of the branched alkyl ester-substituted **DU-3** ($C_{7,2}$) showed the highest crystallinity.

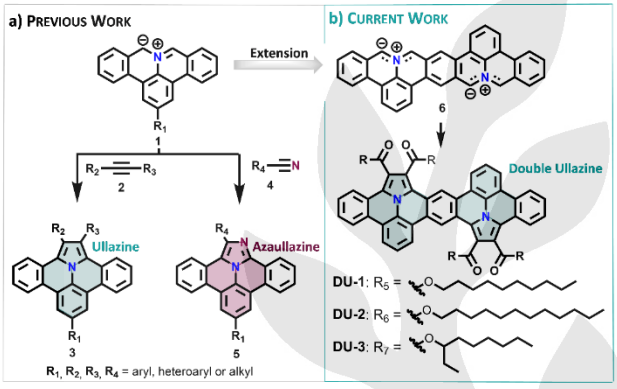

Figure 1 (a) The reported 1,3-dipolar cycloaddition between PAMY (**1**) and alkenes/alkynes (**2**) or nitriles (**4**) to ullazine (**3**) and azaullazine-containing (**5**) PAHs. (b) Concept of the double cycloaddition reaction with PAMY dimer (**6**) to a series of alkyl ester-substituted N-PAHs with a laterally extended double ullazine scaffold **DU-1-3** in this work.

Results and Discussion

The target compounds **DU-1-3** were synthesized starting from the tetra-alcohol species **7** (Scheme 1). The synthesis of **7** was carried out according to our previous synthetic route.[10] The HCl-induced microwave-assisted cyclization of **7** and subsequent hydride abstraction with tritylium tetrafluoroborate gave the iminium salt **8** as crude product.[11] Afterwards, the addition of triethylamine (TEA) to the crude iminium salt and corresponding dipolarophiles (**9**, **10** or **11**) at 60 °C enabled the twofold cycloaddition. The following oxidation with 2,3-dichloro-5,6-dicyano-1,4-benzoquinone (DDQ) provided the target compounds **DU-1-3**, respectively, as yellow solids in yields from 58% for **DU-1** up to 59% for **DU-3** and 61% for **DU-2**, over two steps.[12] All target compounds **DU-1-3** were confirmed by NMR spectroscopy in $C_2D_2Cl_4$ (See SI). The aromatic protons of **DU-1-3** in the ^{1}H-NMR spectrum are assigned to the expected chemical structure by the assistance of two-dimensional NMR spectroscopy, respectively (See SI). Furthermore, **DU-1-3** were characterized by high-resolution (HR) matrix-assisted laser desorption/ionization time of flight (MALDI-TOF) mass spectroscopy (MS). In detail, the MALDI-TOF isotopic distributions of **DU-1-3** are in perfect agreement with the simulated patterns (See SI). Due to the different alkyl ester substitutions, the obtained **DU-1-3** showed a different solubility behavior in common organic solvents, such as dichloromethane (DCM). **DU-1** and **DU-2** with linear C_{10}- and C_{12}-ester substitutions, respectively, provided a low solubility in DCM (0.2 mg/ml). In contrast, **DU-3** with branched $C_{7,2}$ ester substitutions showed an enhanced solubility of up to 3 mg/ml in DCM. Differential scanning calorimetry (DSC) reveals only one peak for all three compounds that is related to the phase transition from crystalline to isotropic phase (SI, Figure S5). The phase transition temperature decreases with longer and more space demanding side chains from 222.4 °C for **DU-1** to 206°C for **DU-2** and 203.8 °C for **DU-3**. Thermogravimetric Analysis (TGA) reveals a high thermal stability of **DU-1-3** up to 260 °C (SI, Figure S6).

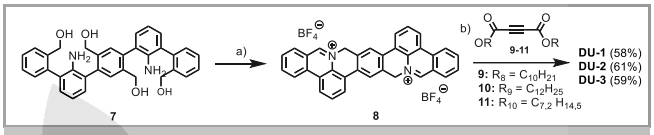

Scheme 1 Synthetic route towards **DU-1-3**. Reagents and conditions: a) i) HCl in 1,4-dioxane (4 M), microwave, argon, 1.5 h; ii) tritylium tetrafluoroborate, acetonitrile, toluene, 90 °C, 2 h. b) i) TEA, chloroform, 60 °C, overnight; ii) DDQ, toluene, r.t., 3 h.

The optoelectronic properties of **DU-1-3** were investigated by UV-Vis absorption and fluorescence spectroscopy in anhydrous DCM. From the UV-Vis absorption and fluorescence spectra, there was no differences between **DU-1**, **DU-2** and **DU-3**, suggesting that the different alkyl ester-substituents do not apparently influence the optoelectronic properties (see SI). Due to the similarity of the optoelectronic properties, only the branched ethylhexyl ester-substituted **DU-3** are exemplarily discussed here. The absorption maximum (λ_{abs}) for **DU-3** was observed at 404 nm with two shoulder peaks at 427 nm and 446 nm (see Figure 2a). The corresponding optical energy gap (ΔE_g) was estimated from the onset of the UV-Vis absorption spectrum and was calculated to be 2.68 eV for **DU-3**. The time-dependent (TD) DFT calculations at the B3LYP/6-31G(d) level fitted the experimental UV-Vis absorption result. The fluorescence spectrum of dimer **DU-3** revealed a fluorescence maximum at 461 nm with a shoulder at 494 nm (Figure 2b). The fluorescence quantum yields varied in the range from 32.9 % for **DU-2** up to 37.6% and 37.7% for **DU-1** and for **DU-3,** respectively.

The electrochemical properties of **DU-1-3** were investigated by cyclic voltammetry (CV) measurements in anhydrous DCM. Due to the different solubility in DCM, the intensities of the CV measurements of **DU-1-3** are diverged (see SI, Figure S4). Due to the similarity, the CV of **DU-3** with the best solubility in DCM are presented in Figure 2c. Compound **DU-3** offered reversible two oxidation waves at 0.3 and 0.5 V versus Fc/Fc$^+$. In comparison to the first two oxidation waves, the third oxidation peak at 0.78 V has a much higher intensity, which presumably indicates the overlap of two closely-spaced oxidation processes or a two-electron oxidation. Nevertheless, a reduction behavior was not observed in the available potential window. The corresponding highest occupied molecular orbital (HOMO) level of **DU-3** was estimated to be -5.1 eV by the half-wave potential of the first reversible oxidation. The lowest unoccupied molecular orbital (LUMO) of **DU-3**, which was determined from the difference between the optical energy gap and electrochemical HOMO, is -2.42 eV. Density functional theory (DFT) and TD-DFT calculations with a Gaussian 09 package were performed for deeper grasp of the electronic ground state. The geometry optimization was carried out *via* the B3LYP level of theory with the 6-31G(d) basis set. The graphical representations of the HOMO and LUMO of **DU-3** are provided in Figure 2d (**DU-1** and **DU-2**: see SI, Figure S11). The HOMO of **DU-3** is completely symmetric and equally delocalized over the full π-system. The DFT-calculated HOMO levels for **DU-1-3** are

in perfect agreement with the experimental HOMO levels derived from the CV measurements (SI, Table S5). In contrast, the distribution of the LUMO shows the main localization between the two ullazine units.

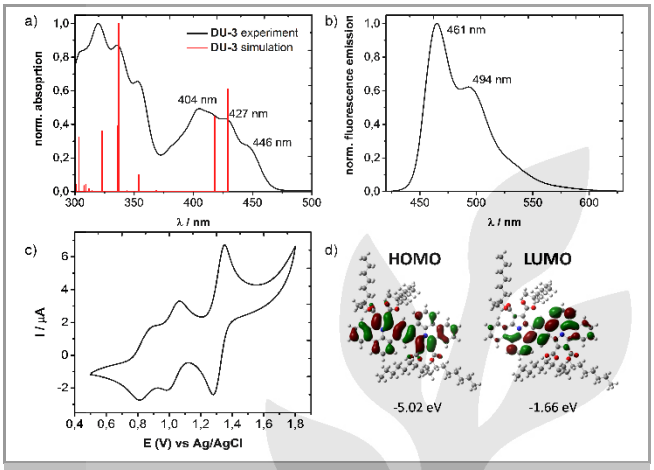

Figure 2 Optoelectronic investigations are exemplarily shown for the best soluble derivative **DU-3.** (a) UV-Vis absorption spectrum of **DU-3** in DCM (black line: experiment; red line: simulations; concentration = 10^{-5} mol/l). (b) Fluorescence emission spectrum of **DU-3** in DCM. (c) Cyclic voltammetry of **DU-3** in DCM with *n*-Bu_4PF_6 as a supporting electrolyte at a scan rate of 75 mV/s. AgCl-coated Ag-wire was used as a reference electrode, platinum as a working electrode and Pt/Ti as a counter electrode. (d) Quantum-chemical DFT calculations of **DU-3** with a B3LYP functional and 6-31G(d) basis set.

Due to the high reversible oxidation behavior of **DU-3**, detailed insight into the cationic species was achieved by spectroelectrochemistry (SEC) *via in-situ* CV, UV-Vis-NIR absorption and EPR spectroscopy in anhydrous DCM (see Figure 3). At low positive potentials, new absorption bands at 493, 570, 1380 and 1689 nm are associated to the formation of the radical cation species (Figure 3a). The appearance of the EPR signal confirmed the formation of the radical cation **DU-3**$^{\bullet+}$. The EPR spectrum of the radical showed a broad unresolved signal with a g-value of 2.0027 (Figure 3c). The DFT calculations demonstrated that the spin density of **DU-3**$^{\bullet+}$ is delocalized over two ullazine motifs in agreement with the shape of the HOMO (Figure 3d). During the second redox process, the intensities of bands centered at 493 and 570 nm increased further and the bands peaked at 1380 and 1689 nm are blue shifted. The EPR signal intensity showed a two-fold increase during the second oxidation process (Figure 3b), indicating that the dication **DU-3**$^{2+}$ may have a diradical character. At the potentials of the third redox event in the CV, the EPR signal intensity decreased and new absorption bands emerged at 531 and 834 nm. This is an indication for the formation of the EPR-silent four positively charged species **DU-3**$^{4+}$.

Figure 4a-c showed the POM images of **DU-1-3** drop-cast films. All layers exhibit birefringence between cross-polarizers and the light intensity of the entire crystals changes from bright to dark by 45° rotation of the substrate. **DU-1** and **DU-2** form a comparable surface morphology with spherulitic domains that are less than 100 micrometers in size. In contrast to **DU-1-2**, **DU-3** forms much larger polycrystalline structures with diameters higher than 100 micrometers. This suggests that the branched substituents improve the film crystallinity and molecular order.

To understand the supramolecular organization of the **DUs**, grazing incidence wide-angle X-ray scattering (GIWAXS) of polycrystalline drop-cast film was performed (Figure 4d-f). The GIWAXS patterns reveal significant differences of the three compounds in crystallinity. All compounds exhibited certain edge-on arrangement on the substrate as indicated by the maximum intensities of the out-of-plane *h00* (according to the Miller index) and in-plane *00l* interstack, as well as π-stacking reflections (*0k0*). The out-of-plane interstack distance is closely related to the length of the substituents and decreased from 2.82 nm for **DU-2** to 2.61 nm for **DU-1**, and 2.20 nm for **DU-3**. This correlation suggests that the long axis of the PAHs is oriented parallel to the surface. **DU-1** and **DU-2** reveal a close π-stacking distance of 0.35 nm, but both are poorly ordered in the in-plane as indicated by a low intensity of the corresponding reflection. Although the molecular interactions might be reduced due to the steric hindrance of the branched substituents,[13] the π-stacking distance of 0.35 nm for **DU-3** remains unchanged. The further equatorial reflection located at q_{xy}=0.47 Å^{-1} and q_z=0 Å^{-1} (Figure 4d) is assigned to the in-plane *00l* interstack distance of 1.33 nm for **DU-1** and **DU-2**, and 1.07 nm for **DU-3**. Since the theoretical molecular length of 1.62 nm calculated by Cerius[2] software is larger, it is assumed that the molecules are arranged in a herringbone structure. As already observed by POM, the crystallinity of **DU-3** is improved in comparison to **DU-1-2** as evidenced by the additional high intensity reflections. In summary of the structural study, it can be concluded that the introduction of branched side chains in **DU-3** enhances the self-assembly and crystallinity.

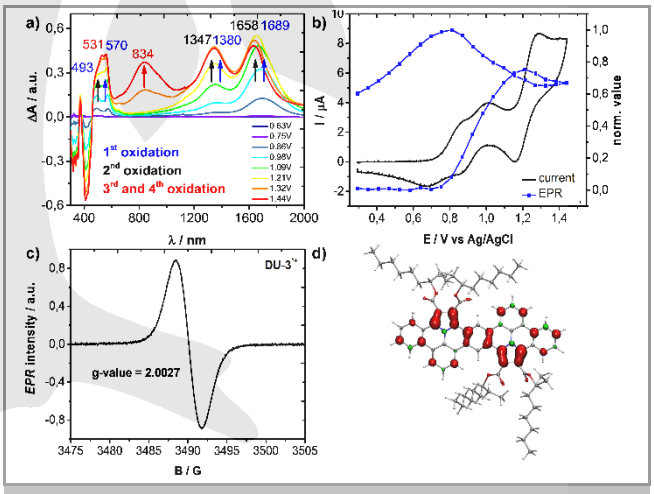

Figure 3 *In situ* EPR/UV-Vis-NIR spectroelectrochemistry of the oxidation of **DU-3**. (a) UV-Vis-NIR spectra measured during the electrochemical oxidation of **DU-3** (blue arrows and numbers: first oxidation; black arrows and numbers: second oxidation and red arrows and numbers: third and fourth oxidation). (b) Cyclic voltammogram (black line) and potential dependence of normalized EPR intensity (blue line). (c) Experimental EPR spectrum of radical cation species **DU-3**$^{\bullet+}$. (d) DFT-computed spin density distribution of **DU-3**$^{\bullet+}$.

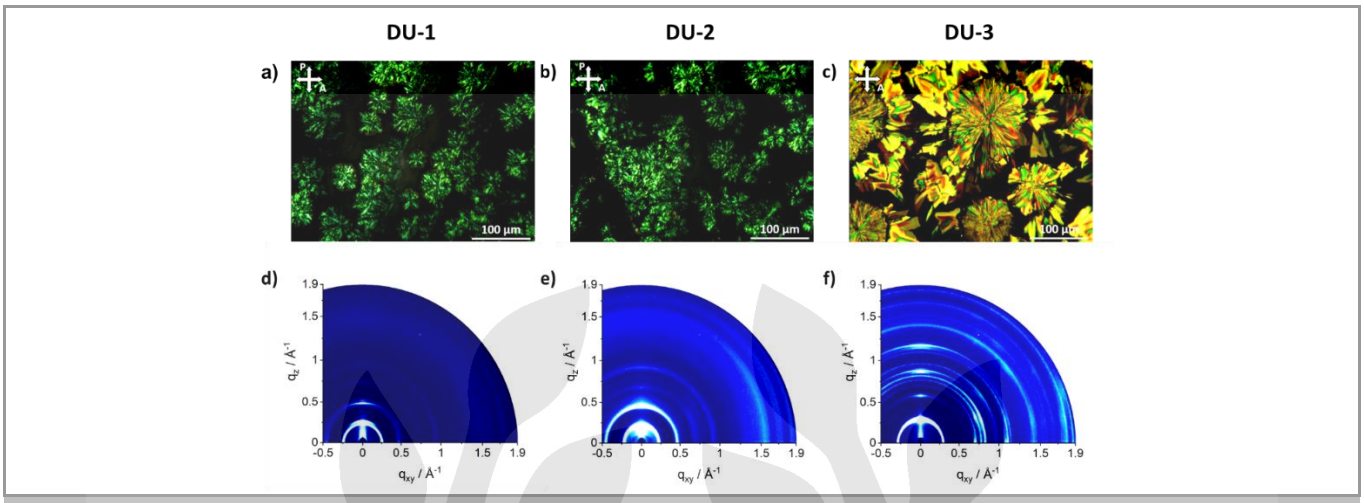

Figure 4 POM images and GIWAXS patterns of **DU-1** (a,d), **DU-2** (b,e) and **DU-3** (c,f) drop-cast films.

Conclusion

In summary, we have synthesized a series of alkyl ester-substituted *N*-PAHs with a laterally extended double ullazine scaffold (**DU-1-3**). As key step for the synthesis, the first example of the double cycloaddition between PAMY-dimer (**6**) and different electron-deficient dipolarophiles were presented. Interestingly, the CV measurements for **DU-1-3** revealed a highly reversible oxidation potential and confirmed up to three oxidation waves. The corresponding different oxidized species of **DU-3** were investigated by *in situ* EPR measurements and UV-Vis-NIR spectroscopy. It was shown that the radical species with the pronounced absorption bands in the near infrared region are formed. Additionally, the self-assembly of the different alkyl ester-substituted **DU-1-3** was investigated by POM and GIWAXS. In contrast to linear alkyl ester-substituted derivatives (**DU-1** and **DU-2**), the branched ethylhexyl ester-substituted compound (**DU-3**) revealed higher order of the self-assembled structure. We believe that the cycloaddition of the double-ullazine based PAHs could pave the way for the synthesis of unprecedented extended *N*-PAHs or *N*-doped graphene nanoribbons.

Funding Information

This research was financially supported by the EU Graphene Flagship (Graphene Core 3, 881603), ERC Consolidator Grant (T2DCP, 819698), the German Research Foundation (DFG) within the Cluster of Excellence "Center for Advancing Electronics Dresden (cfaed)" and DFG-NSFC Joint Sino-German Research Project (EnhanceNano, No. 391979941), as well as the DFG-SNSF Joint Switzerland-German Research Project (EnhanTopo, No. 429265950). M. Borkowski and T. Marszalek acknowledge the Foundation for Polish Science financed by the European Union under the European Regional Development Fund (POIR.04.04.00-00-3ED8/17). W. Pisula acknowledges National Science Centre, Poland, through the grant UMO-2015/18/E/ST3/00322.

Acknowledgment

We thank F. Drescher, Dr. S. Machill, Prof. E. Brunner and Dr. T. Lübken for HR-MS measurements and NMR measurements, respectively. We also thank M. Sc. Felix Fries and Prof. Sebastian Reineke for PLQY measurements. We thank the Center for Information Services and High Performance Computing (ZIH) at TU Dresden for generous allocations of compute resources. Moreover, we thank M. Sc. Felix Fries and Prof. Sebastian Reineke for PLQY measurements.

Supporting Information

Yes

Primary Data

NO

References and Notes

(1) (a) A. Narita, X.-Y. Wang, X. Feng, K. Müllen, *Chem. Soc. Rev.* **2015**, 44, 6616-6643. (b) J. Liu, X. Feng, *Angew. Chem. Int.* Ed. **2020**, 59, 52, 23386-23401.

(2) X.-Y. Wang, A. Narita, K. Müllen, *Nat. Rev. Chem.* **2017**, 2, 0100.

(3) (a) J. Liu and X. Feng, *Synlett*, **2020**, 31, 211-222. (b) L. Ji, A. Friedrich, I. Krummenacher, A. Eichhorn, H. Braunschweig, M. Moos, S. Hahn, F. L. Geyer, O. Tverskoy, J. Han, C. Lambert, A. Dreuw, T. B. Marder, U. H. F. Bunz, *J. Am. Chem. Soc.* **2017**, 139, 15968-15976. (c) M. Takase, V. Enkelmann, D. Sebastiani, M. Baumgarten. K. Müllen, Angew. *Chem. Int. Ed.* **2007**, 46, 5524-5527.

(4) (a) J. H. Delcamp, A. Yella, T. W. Holcombe, M. K. Nazeeruddin, M. Grätzel, *Angew. Chem. Int. Ed.* **2013**, 52, 376-380. (b) H. Qiao, Y. Deng, R. Peng, G. Wang, J. Yuan, S. Tan, *RSC Adv.* **2016**, 6, 70046-70055. (c) S. Mathew, N. A. Astani, B. F. E. Curchod, J. H. Delcamp, M. Marszalek, J. Frey, U. Rothlisberger, M. K. Nazeeruddin, M. Grätzel, *J. Mater. Chem. A* **2016**, 4, 2332-2339. (d) C. Cebrián, J. Mater. *Chem. C* **2018**, 6, 11943-11950.

(5) H. Balli, M. Zeller, *Helv. Chim. Acta* **1983**, 66, 2135-2139.

(6) (a) G. Zhang, P. Gautam, J. M. W. Chan, *Org. Chem. Front.* **2020**, 7, 787-795. (b) A. Das, I. Ghosh, B. König, *Chem. Commun.* **2016**, 52, 8695-8698. (c) D. Wan, X. Li, R. Jiang, B. Feng, J. Lan, R. Wang, J. You, *Org. Lett.* **2016**, 18, 2876-2879. (d) S. Boldt, S. Parpart, A. Villinger, P. Ehlers, P. Langer, *Angew. Chem. Int. Ed.* **2017**, 56, 4575-4578.

(7) (a) R. Berger, M. Wagner, X. Feng, K. Müllen, *Chem. Sci.* **2015**, 6, 436-441. (b) X.-Y. Wang, M. Richter, Y. He, J. Björk, A. Riss, R. Rajesh, M. Garnica, F. Hennersdorf, J. J. Weigand, A. Narita, R. Berger, X. Feng, W. Auwärter, J. V. Barth, C.-A. Palma, K. Müllen, *Nat. Commun.* **2017**, 8, 1948.

(8) (a) M. Richter, K. S. Schellhammer, P. Machata, G. Cuniberti, A. Popov, F. Ortmann, R. Berger, K. Müllen, X. Feng, *Org. Chem. Front.* **2017**, 4, 847-852. (b) M. Richter, S. Hahn, E. Dmitrieva, F. Rominger, A. Popov, U. H. F. Bunz, X. Feng, R. Berger, *Chem. Eur. J.* **2019**, 25, 1345-1352. (c) S. Ito, Y. Tokimaru and K. Nozaki, *Angew. Chem.* **2015**, 127, 7364-7368.

(9) (a) A. Riss, M. Richter, A. P. Paz, X.-Y. Wang, R. Raju, Y. He, J. Ducke, E. Corral, M. Wuttke, K. Seufert, M. Garnica, A. Rubio, J. V. Barth, A. Narita, K. Müllen, R. Berger, X. Feng, C.-A. Palma, W. Auwärter, *Nat. Commun.* **2020**, 11, 1490. (b) Q.-Q. Li, K. Ochiai, C.-A. Lee, S. Ito, *Org. Lett.* **2020**, 22, 6132-6137.

(10) (a) R. Berger, A. Giannakopoulos, P. Ravat, M. Wagner, D. Beljonne, X. Feng, K. Müllen, *Angew. Chem. Int. Ed.* **2014**, 53, 10520-10524. (b) R. Berger, A. Giannakopoulos, P. Ravat, M. Wagner, D. Beljonne, X. Feng, K. Müllen, *Angew. Chem.* **2014**, 126, 10688-10692.

(11) **Synthetic procedure for iminum-salt (8):** In a microwave tube, the tetra-alcohol species (**7**, 0.1 g, 188 µmol.) was added into a stirring anhydrous hydrogen chloride solution (4 M in dioxane, 5 ml). The microwave tube was capped and placed in a microwave reactor. A dynamic mode was chosen (300 W, power max: on, activated cooling, pre-stirring: 10 seconds, temperature: 130 °C) for 1.5 h. After cooling to room temperature the cap was removed and the reaction mixture was transferred to a round-bottom flask. The solvents were removed under reduced pressure. The crude product was dissolved in toluene (anhydrous, 20 ml) and heated to 90 °C under argon. In a second dry and inert Schlenk-flask, triphenylcarbenium tetrafluoroborate was dissolved in anhydrous acetonitrile and added dropwise. After continuous stirring for 2 hours, the solvents were removed under reduced pressure. The residue was dissolved in DCM and precipitated in diethylether (250 mL). The crude product **8** was obtained as yellow solid. **HR-MS (MALDI-ToF):** m/z ($[M+H]^+$) = 459.1893, calcd. for $C_{34}H_{23}N_2$: m/z = 459.1861, error = 6.96 ppm.

(12) **General synthetic procedure of DU-1-3:** In dry and inert Schlenk-flask, crude **8** (100 mg) and the corresponding dipolarophiles were dissolved in anhydrous chloroform. At 60 °C, the addition of triethylamine was carried out in one shot and the reaction mixture was done under continuous stirring overnight. After the cooling to room temperature, the reaction mixture was transferred into round-bottom flask and the solvent was removed under reduced pressure. After the addition of 2,3-dichloro-5,6-dicyano-1,4-benzoquinone (DDQ) the round-bottom flask was sealed and purged with argon. Anhydrous toluene was added and the reaction mixture was stirred for three hours. The reaction was quenched with water and extracted with dichloromethane (50 ml, 5 times). The solvent was removed under reduced pressure. The crude product was dissolved in a small amount of dichloromethane and precipitated in methanol (250 ml). After the filtration, the crude product was purified by column chromatography on silica in pure chloroform and via rGPC. The target compounds **DU-1-3** were obtained as yellow solids.

DU-1: ^{1}H-NMR (600 MHz, $C_2D_2Cl_4$): δ 9.71 (s, 2H), 8.25 (d, *J* = 8.2 Hz, 2H), 8.19 (d, *J* = 8.0 Hz, 2H), 8.01 (d, *J* = 8.0 Hz, 2H), 7.89 (d, *J* = 8.0 Hz, 2H), 7.58 (t, *J* = 7.7 Hz, 2H), 7.32 (t, *J* = 7.5 Hz, 2H), 7.23 (t, *J* = 7.3 Hz, 2H), 4.49 (t, *J* = 7.0 Hz, 4H), 4.42 (t, *J* = 7.0 Hz, 4H), 1.83 (td, *J* = 14.5, 7.2 Hz, 12H), 1.53 – 1.40 (m, 8H), 1.38 – 1.30 (m, 8H), 1.29 – 1.25 (m, 4H), 1.24 – 1.12 (m, 40H), 0.77 (dt, *J* = 21.0, 7.0 Hz, 12H). ^{13}C-NMR (151 MHz, $C_2D_2Cl_4$): δ 167.2, 166.2, 128.6, 128.0, 127.9 127.6, 125.7, 125.6, 124.6, 123.8, 123.0, 122.1, 122.0, 121.4, 32.2, 30.0, 29.9, 29.8, 29.7, 29.2, 29.0, 26.5, 23.0, 14.5. HR-MS (MALDI-ToF): m/z ($[M]^+$) = 1240.7471, calcd. for $C_{82}H_{100}N_2O_8$: m/z = 1240.7479, error = -0.7 ppm. IR: $\tilde{\nu}$ = 2921, 2853, 1713, 1195, 1128, 747 cm^{-1}.

DU-2: ^{1}H-NMR (600 MHz, $C_2D_2Cl_4$): 9.54 (s, 2H), 8.10 (d, *J* = 7.5 Hz, 2H), 8.04 (d, *J* = 7.6 Hz, 2H), 7.85 (d, *J* = 7.3 Hz, 2H), 7.72 (d, *J* = 7.2 Hz, 2H), 7.47 (t, *J* = 7.2 Hz, 2H), 7.21 (t, *J* = 7.0 Hz, 2H), 7.10 (t, *J* = 6.5 Hz, 2H), 4.48 – 4.40 (m, 7H), 4.40 – 4.27 (m, 8H), 1.79 (d, *J* = 6.8 Hz, 8H), 1.42 (d, *J* = 6.1 Hz, 8H), 1.37 – 1.25 (m, 8H), 1.12 (dd, *J* = 28.9, 25.8 Hz, 60H), 0.72 (dd, *J* = 16.3, 6.8 Hz, 12H). ^{13}C-NMR (151 MHz, $C_2D_2Cl_4$): δ 167.54, 166.39, 128.55, 127.94, 127.87, 126.50, 126.22, 125.64, 124.50, 124.07, 123.80, 123.42, 122.26, 122.20, 122.03, 121.32, 120.57, 120.07, 74.20, 32.20, 30.02, 30.00, 29.98, 29.93, 29.80, 29.67, 29.16, 29.03, 26.55, 26.52, 23.00, 14.51, 14.50. HR-MS (MALDI-ToF): m/z ($[M]^+$) = 1352.8741, calcd. for $C_{90}H_{116}N_2O_8$: m/z = 1352.8731, error = 0.7 ppm. IR: $\tilde{\nu}$ = 2918, 2851, 1713, 1194, 1126, 747 cm^{-1}.

DU-3: ^{1}H-NMR (600 MHz, $C_2D_2Cl_4$): δ 9.78 (s, 2H), 8.39 (dd, *J* = 24.5, 6.4 Hz, 4H), 8.24 (d, *J* = 6.7 Hz, 2H), 8.16 (s, 2H), 7.69 (t, *J* = 7.5 Hz, 2H), 7.42 (s, 4H), 5.28 – 5.21 (m, 2H), 5.17 – 5.04 (m, 2H), 1.86 – 1.61 (m, 20H), 1.34 (d, *J* = 37.1 Hz, 12H), 1.26 – 1.14 (m, 12H), 1.08 (d, *J* = 2.8 Hz, 8H), 1.01 – 0.89 (m, 12H), 0.81 (d, *J* = 1.1 Hz, 6H), 0.66 (d, *J* = 6.2 Hz, 6H). ^{13}C-NMR (151 MHz, $C_2D_2Cl_4$): δ 166.84, 166.79, 128.82, 128.68, 128.17, 127.11, 126.64, 126.62, 125.73, 125.72, 125.26, 125.24, 125.22, 124.67, 124.24, 124.14, 123.78, 123.27, 123.25, 122.87, 122.31, 122.29, 121.77, 120.13, 120.10, 116.85, 114.87, 114.38, 114.35, 74.20, 33.56, 33.46, 32.91, 32.11, 32.00, 29.80, 29.67, 26.83, 26.17, 25.72, 25.51, 22.98, 22.89, 14.51, 14.37, 10.06, 9.82. HR-MS (MALDI-ToF): m/z ($[M]^+$) = 1184.6855, calcd. for $C_{78}H_{92}N_2O_8$: m/z = 1184.6853, error = 0.1 ppm. IR: $\tilde{\nu}$ = 2954, 2924, 2858, 1703, 1194, 744 cm^{-1}.

(13) I. Osaka, R. Zhang, G. Sauvé, D.-M. Smilgies, T. Kowalewski, R. D. McCullough, *J. Am. Chem. Soc.* **2009**, 131, 2521-2529.

Electronic Supplementary Information (ESI)

Synthesis and Self-Assembly Behavior of Double Ullazine-Based Polycyclic Aromatic Hydrocarbons

Marcus Richter, Michal Borkowski, Yubin Fu, Evgenia Dmitrieva, Alexey Popov, Ji Ma, Tomasz Marszalek, Wojciech Pisula, Xinliang Feng

*Corresponding Author E-Mail: xinliang.feng@tu-dresden.de

Table of Content

1) General Information

Unless otherwise stated, the commercially available reagents and dry solvents were used without further purification. The reactions were performed using standard vacuum-line and Schlenk techniques, work and purification of all compounds were performed under air and with reagent-grade solvents. Column chromatography was done with silica gel (particle size 0.063-0.2 mmm from VWR) and silica coated aluminum sheets with fluorescence indicator from Merck were used for thin layer chromatography. Purification by recycling gel permeation chromatography (rGPC) was performed on JAI HPLC LC 9110 II NEXT with fraction collector FC- 3310 and GPC columns 2H and 1H (connected in series). The rGPC was used with HPLC-grade chloroform at room temperature.

For microwave-assisted reactions a CEM Discover-SP was used.

NMR Data were recorded on a Bruker AV-III 600 spectrometer operating at 600 MHz for 1H and 151 MHz for 13C with standard Bruker puls programs at room temperature. Chemical shifts δ are given in ppm relative to TMS, coupling constants J are given in Hertz. $C_2D_2Cl_4$ ($\delta(^1H)$ = 5.91 ppm, $\delta(^{13}C)$ = 74.2 ppm), C_2D_6OS ($\delta(^1H)$ = 2.50 ppm, $\delta(^{13}C)$ = 39.56 ppm) and $CDCl_3$ ($\delta(^1H)$ = 7.26, $\delta(^{13}C)$ = 77.16 ppm) was used as solvent, lock and internal standard.

High-Resolution- (HR) matrix-assisted laser-desorption ionization time of flight (MALDI-TOF) spectra were recorded on a Bruker Autoflex Speed MALDI-TOF MS (Bruker Daltonics, Bremen, Germany) with dithranol or trans-2-[3-(4-*tert*-butylphenyl)-2-methyl-2-propenylidene]malononitrile (DCTB) as the matrix. The preparation of the sample was performed in solid state.

HR-atmospheric pressure chemical ionization (APCI) mass spectra and HR-electrospray ionization (ESI) mass spectra were recorded with Agilent 6538 Ultra High Definition (UHD) Accurate-Mass Q-TOF LC/MC system using the positive mode.

Differential scanning calorimetry (DSC) measurements were recorded at 5 K per minute with the Mettler Toldeo SC 1 with intracooler.

TGA measurements were recorded on Mettler-Toledo TGA 1 SF 1100 with a 70 ml AlOx crucible under nitrogen atmosphere.

Infrared (IR) spectra are reported as solid phase measurement in wavenumbers (cm^{-1}). The IR measurements were recorded on Bruker Tensor II with a diamond ATR unit.

UV-Vis absorption spectroscopy was conducted on an Agilent Technologies Cary Series 5000 by using a 10 mm optical-path quartz cell at room temperature. Unless otherwise noted, a concentration of 10^{-5} mol/l in DCM was used for absorption between 0.1 and 1 at the wavelength region of experimental interest. Solution fluorescence spectra were recorded on a Perkin Elmer Fluorescence Spectrometer LS 55 at room temperature. Solution fluorescence spectra were recorded in argon-purged solutions at concentrations of 10^{-5} mol/l in anhydrous DCM. All measurements were carried out in a 10 mm fluorescence quartz cell at room temperature.
The photoluminescence quantum yields were recorded via integrating-sphere method.[1] The measurement carried out with a 340 nm LED source from Thorlabs, integrating sphere from Labsphere and an CAS 140CT spectrometer from Instrument Systems.

Cyclic Voltammetry was carried out on a CHI760 E potentiostat (CH Instruments, USA) in a three-electrode cell in a DCM solution of tetrabutylammonium hexafluorophosphate (n-Bu_4NPF_6) (0.1 M) with a scan rate of 75 mV/s at room temperature. All measurements were recorded in argon-purged solutions in anhydrous DCM. AgCl-coated Ag-wire was used as a reference electrode, platinum as a working electrode and Pt/Ti as a counter electrode. The oxidation potential for ferrocene $E_{Fe/Fe+}$ in DCM was observed at 0.52 eV.[2]
In situ EPR/UV–Vis–NIR spectroelectrochemical experiments were performed in the optical EPR cavity (ER 4104OR, Bruker Germany).[3] EPR spectra were recorded by the EMX X-band CW spectrometer (Bruker, Germany). UV–Vis–NIR spectra were measured using the Avantes spectrometer AvaSpec-2048x14-USB2 with the CCD detector and AvaSpec-NIR256-2.2 with the InGaAs detector applying the AvaSoft 7.5 software. For electron excitation, halogen lamp Avantes Avalight-Hal-S was used. Both, the EPR spectrometer and the UV–Vis–NIR spectrometer are linked to a HEKA potentiostat PG 390 which triggers both spectrometers. Triggering is performed by the software package PotMaster v2x40 (HEKA Electronik, Germany). For standard in situ EPR/ UV–Vis–NIR spectroelectrochemical experiments, an EPR flat cell was used. A laminated platinum mesh as the working electrode, a silver chloride coated silver wire as the pseudo-reference electrode, and a platinum wire as the counter electrode were used in spectroelectrochemical experiments. 0.1 M n-BuN_4PF_6 in diclorometane was used as a supporting electrolyte.

All density functional theory (DFT) and time-dependent DFT (TD-DFT) calculations were performed using the Gaussian 09 program.[4] The geometry optimization in the ground state was optimized by the B3LYP functional with the 6-31G(d) basis set. Geometry optimization was done in the gas phase. In order to simulate the UV-Vis spectra of the molecules, TD-DFT

calculations at the B3LYP/6-31G(d) level of theory were performed. For better comparison of the experimental absorption spectra, the polarity of the solvent dichloromethane was added.

2) Experimental Section

Synthesis and analytical data of 1,5-dibora-2,6-dioxa-*sym*-hydrindacene-1,5-diol (**S2**) are provided in our previous work.[5] Didecyl but-2-ynedioate (**4**) and didodecyl but-2-ynedioate (**5**) were prepared according to the literatures.[6]

Synthesis of 2-bromo-6-(1'-hydroxymethylphenyl))-aniline (S3)

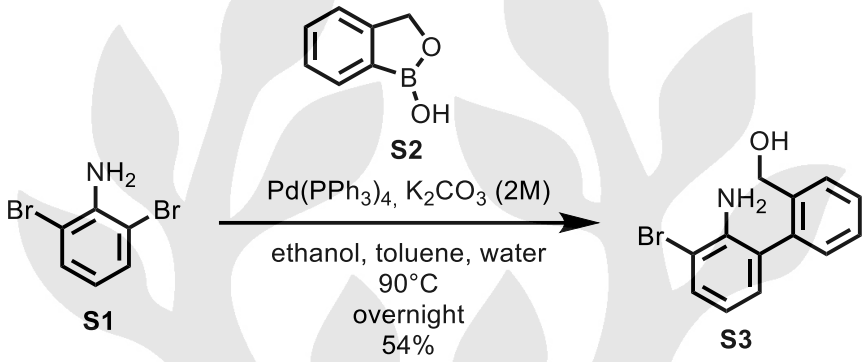

A solution of 2,6-dibromoaniline (**S1**, 4 g, 16 mmol, 1.1 eq.) and 1-hydroxy-3H-2,1-benzoxaborole (**S2,** 1.95g , 14.5 mmol, 1.0 eq.) in a mixture of toluene (320 ml), ethanol (64 ml) and 2 M potassium carbonate solution (124 ml) was purged with argon for 30 min. After the addition of tetrakis(triphenylphosphine)palladium(0) (1.67 g. 1.45 mmol, 10 mol-%) the mixture was refluxed in an oil bath overnight at 90 °C. The reaction mixture was allowed to reach room temperature and the organic layer was separated. The aqueous phase was extracted three times with diethylether and the combined organic layers were washed with brine and dried over magnesium sulfate. The solvent was removed under reduced pressure and the residue was purified by column chromatography on silica (*i*-hexane: ethyl acetate: 7:3) to afford 2-bromo-6-(1'-hydroxymethylphenyl))-aniline (**S3**) in 54% yield.

2-Bromo-6-(1'-hydroxymethylphenyl))-aniline (**S3**)

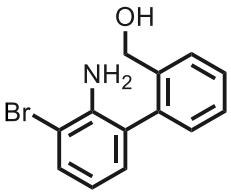

S3

S3: R_f = 0.4 (SiO_2; *i*-hexane/EA = 7:3). Mp = 257 °C. Yield = 54%.

^{1}H-NMR (600 MHz, DMSO-d$_6$): δ 7.64 – 7.59 (m, 1H), 7.45 – 7.39 (m, 2H), 7.34 (td, *J* = 7.5, 1.0 Hz, 1H), 7.11 (dd, *J* = 7.5, 1.2 Hz, 1H), 6.90 (dd, *J* = 7.4, 1.4 Hz, 1H), 6.65 – 6.56 (m, 1H), 5.07 (t, *J* = 5.3 Hz, 1H), 4.44 (s, 2H), 4.26 (ddd, *J* = 32.5, 13.7, 5.3 Hz, 2H).

^{13}C-NMR (151 MHz, DMSO-d$_6$): 142.3, 140.6, 136.1, 131.6, 129.5, 129.4, 128.0, 127.3, 127.2, 126.8, 117.8, 108.3, 60.4

HR-MS (ESI-MS): m/z ([M+H]$^+$) = 278.0173, calcd. for $C_{13}H_{13}BrNO$: m/z = 278.0180, error = - 2.5 ppm

IR: $\tilde{\nu}$ = 3459, 3373, 1605, 1443, 1042, 730 cm^{-1}

Synthesis of (2',2'''-diamino-[1,1':3',1'':4'',1''':3''',1''''-quinquephenyl]-2,2'',2'''',5''-tetrayl)tetramethanol (7)

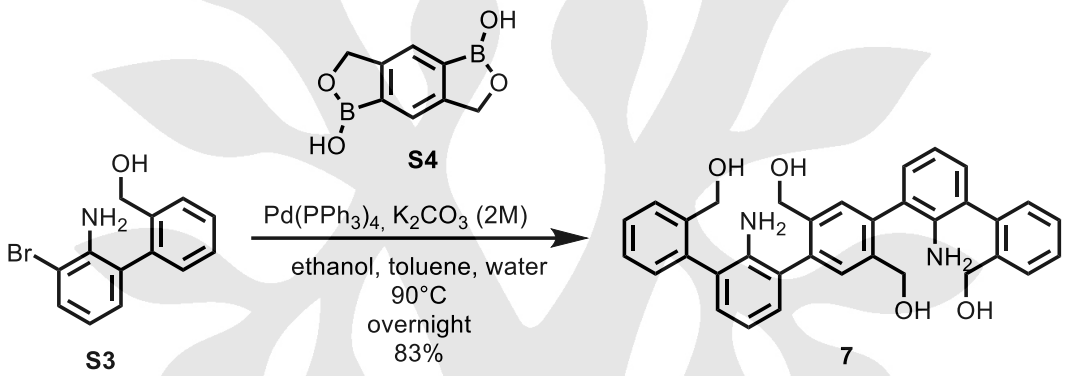

A solution of 2-bromo-6-(1'-hydroxymethylphenyl))-aniline (**S3,** 3 g, 10.8 mmol, 2.05 eq.) and 1,5-dibora-2,6-dioxa-*sym*-hydrindacene-1,5-diol (**S4**, 1 g, 5.3 mmol, 1.0 eq.) in a mixture of toluene (150 ml). ethanol (70 ml) and 2 M potassium carbonate solution (90 ml) was purged with argon for 30 min. After the addition of tetrakis(triphenylphosphine)palladium(0) (0.3 g, 263 µmol, 5 mol-%) the mixture was refluxed in an oil bath overnight at 90 °C. The reaction mixture was allowed to reach room temperature and the organic layer was separated. The aqueous phase was extracted three times with dichloromethane and the combined organic layers were washed with brine and dried over magnesium sulfate. The solvent was removed under reduced pressure. The residue was dissolved in a minimum amount of DCM (~15 mL) and precipitated in toluene (300 ml). The precipitated solid was filtered and compound **7** was obtained as white solid in 83% yield.

(2',2'''-Diamino-[1,1':3',1":4",1''':3''',1''''-quinquephenyl]-2,2",2'''',5"-tetrayl)tetramethanol (**7**)

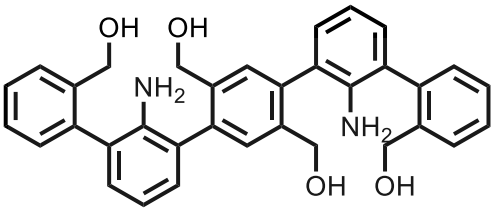

7

7: Mp = 214 °C. Yield = 83%.

^{1}H-NMR (600 MHz, DMSO-d$_6$): δ 7.69 – 7.57 (m, 2H), 7.48 – 7.30 (m, 6H), 7.23 – 7.12 (m, 2H), 7.03 – 6.96 (m, 2H), 6.95 – 6.86 (m, 2H), 6.83 – 6.66 (m, 2H), 5.19 – 4.89 (m, 4H), 4.60 – 4.18 (m, 8H), 3.80 (dd, *J* = 73.5, 16.1 Hz, 4H).

^{13}C-NMR (151 MHz, DMSO-d$_6$): δ 141.93, 141.91, 141.85, 140.98, 140.95, 140.73, 140.66, 139.41, 139.25, 139.19, 137.02, 136.84, 136.83, 136.70, 135.68, 129.83, 129.63, 129.22, 129.16, 129.13, 129.11, 129.00, 128.25, 128.16, 128.04, 127.60, 127.59, 127.55, 127.19, 127.02, 126.84, 125.62, 125.60, 125.58, 125.53, 125.42, 125.42, 116.83, 116.67, 116.55, 116.53, 116.42, 60.56, 60.52, 60.44, 60.37, 60.34, 60.26, 60.24.

HR-MS (ESI-MS): m/z ([M+H)$^+$] = 533.2432, calcd. for $C_{34}H_{33}N_2O_4$: m/z = 533.2440, error = - 1.5 ppm

IR: $\tilde{\nu}$ = 3357, 3259, 1609, 1438,1039, 754 cm^{-1}

Hydrogen bonds between amino and hydroxyl substituents hinder free rotation of the phenyl substituents. This causes isomer formation and explains the complex ^{1}H- and ^{13}C-spectra.

Synthesis of 8,21-dihydroisoquinoline[4',3',2':8,1]quinoline[4,3-*j*]isoquinolino[4,3,2-*de*]phenanthridine-9,20-diium (8)

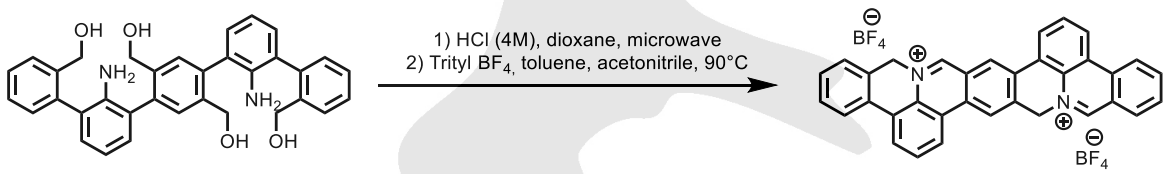

7 **8**

In a microwave tube, the tetra-alcohol species (**7**, 0.1 g, 188 µmol.) was added into a stirring anhydrous hydrogen chloride solution (4 M in dioxane, 5 ml). The microwave tube was capped and placed in a microwave reactor. A dynamic mode was chosen (300 W, power max: on, activated cooling, pre-stirring: 10 seconds, temperature: 130 °C) for 1.5 h. After cooling to room temperature the cap was removed and the reaction mixture was transferred to a round-

bottom flask. The solvents were removed under reduced pressure. The crude product was dissolved in toluene (anhydrous, 20 ml) and heated to 90 °C under argon. In a second dry and inert Schlenk-flask, triphenylcarbenium tetrafluoroborate was dissolved in anhydrous acetonitrile and added dropwise. After continuous stirring for 2 hours, the solvents were removed under reduced pressure. The residue was dissolved in DCM and precipitated in diethylether (250 mL). The crude product **8** was obtained as yellow solid.

8,21-Dihydroisoquinoline[4',3',2':8,1]quinoline[4,3-*j*]isoquinolino[4,3,2-*de*]phenanthridine-9,20-diium (**8**)

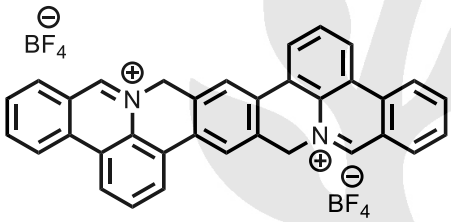

8

HR-MS (MALDI-ToF): m/z ($[M+H]^+$) = 459.1893, calcd. for $C_{34}H_{23}N_2$: m/z = 459.1861, error = 6.96 ppm.

Esterification of acetylenedicarboxylic acid to di(nonan-3-yl)but-2-ynedioate (11)

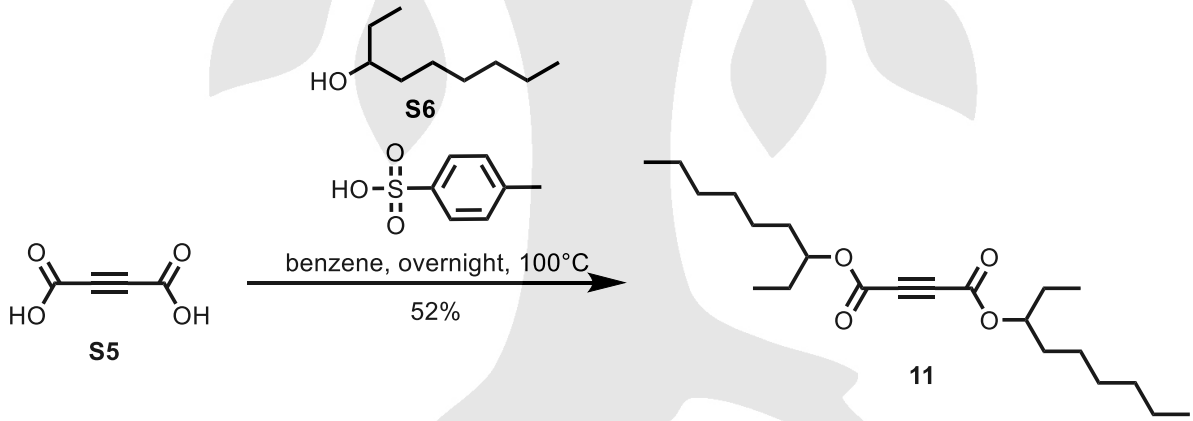

In a dry Schlenk-flask, acetylenedicarboxylic acid (**S5**, 3 g, 26.5 mmol, 1.0 eq.), *p*-toluene sulfonic acid (455 mg, 2.65 mmol, 0.1 eq.) and 3-nonanol (**S6**, 8.4 g, 58 mmol, 2.20 eq.) were dissolved in 60 ml dry benzene and heated under reflux overnight with a dean-Stark apparatus. After the quenching with water and extraction with dichlormethane (30 ml, 3 times), the crude product was purified by column chromatography on silica in pure *i*-hexane. The di(nonan-3-yl)but-2-ynedioate (**11**) was obtained as colourless liquid in 52% yield.

Di(nonan-3-yl)but-2-ynedioate (**11**)

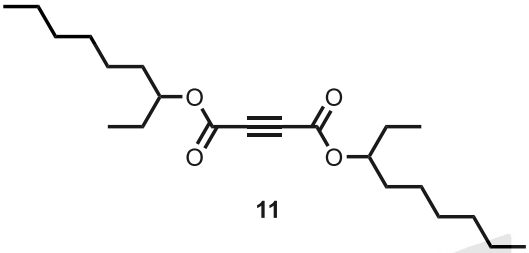

11

11: R_f = 0.6 (SiO_2; *i*-hexane). Mp: 285 °C. Yield = 52%.

^{1}H-NMR (300 MHz, $CDCl_3$): δ 5.04 – 4.84 (m, 2H), 1.72 – 1.47 (m, 8H), 1.27 (s, 16H), 0.89 (dt, *J* = 9.1, 7.2 Hz, 12H).

^{13}C-NMR (75 MHz, $CDCl_3$): δ 152.07, 79.48, 75.00, 33.47, 31.79, 29.20, 26.90, 25.28, 22.69, 14.17, 9.62.

HR-MS: The mass measurement for compound **11** via APCI (positive and negative ionization), ESI (positive and negative ionization) and MALDI-TOF was not successful.

IR: $\tilde{\nu}$ = 2928, 2857, 1716, 1245, 1021 cm^{-1}.

General Synthesis of DU-1-3

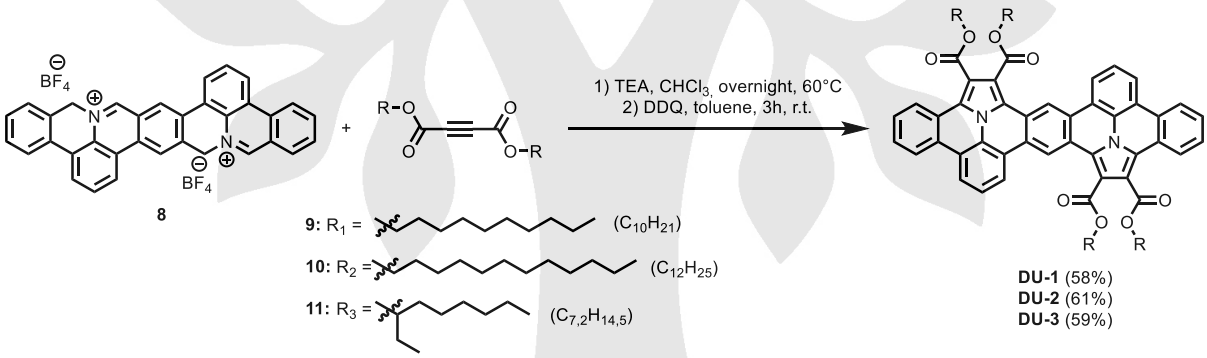

In dry and inert Schlenk-flask, crude **8** (100 mg) and the corresponding dipolarophiles were dissolved in anhydrous chloroform. At 60 °C, the addition of triethylamine was carried out in one shot and the reaction mixture was done under continuous stirring overnight. After the cooling to room temperature, the reaction mixture was transferred into round-bottom flask and the solvent was removed under reduced pressure. After the addition of 2,3-dichloro-5,6-dicyano-1,4-benzoquinone (DDQ) the round-bottom flask was sealed and purged with argon. Anhydrous toluene was added and the reaction mixture was stirred for three hours. The reaction was quenched with water and extracted with dichloromethane (50 ml, 5 times). The solvent was removed under reduced pressure. The crude product was dissolved in a small amount of

dichloromethane and precipitated in methanol (250 ml). After the filtration, the crude product was purified by column chromatography on silica in pure chloroform and via rGPC. The target compounds **DU-1-3** were obtained as yellow solids.

Tetradecylbenzo[7',8']indolizino[6',5',4',3':8,1,2]isoquinolino[4,3-*j*]benzo[7,8]indolizino[6,5,4,3-*def*]phenanthridine-1,2,11,12-tetracarboxylate (**DU-1**)

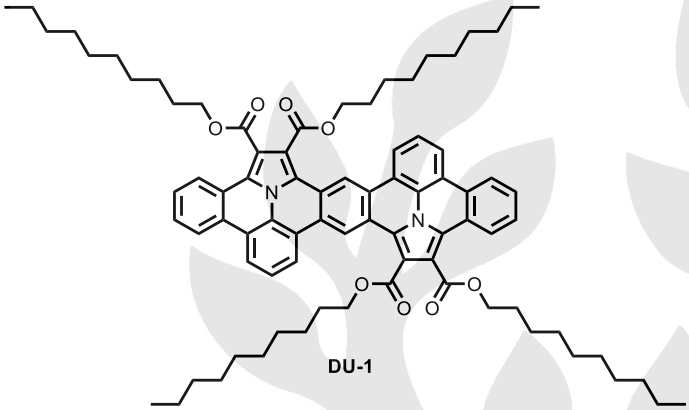

DU-1: R_f = 0.1 (SiO_2; DCM). Mp: 222.4 °C. Yield = 59% over 2 steps.

^{1}H-NMR (600 MHz, $C_2D_2Cl_4$): δ 9.71 (s, 2H), 8.25 (d, *J* = 8.2 Hz, 2H), 8.19 (d, *J* = 8.0 Hz, 2H), 8.01 (d, *J* = 8.0 Hz, 2H), 7.89 (d, *J* = 8.0 Hz, 2H), 7.58 (t, *J* = 7.7 Hz, 2H), 7.32 (t, *J* = 7.5 Hz, 2H), 7.23 (t, *J* = 7.3 Hz, 2H), 4.49 (t, *J* = 7.0 Hz, 4H), 4.42 (t, *J* = 7.0 Hz, 4H), 1.83 (td, *J* = 14.5, 7.2 Hz, 12H), 1.53 – 1.40 (m, 8H), 1.38 – 1.30 (m, 8H), 1.29 – 1.25 (m, 4H), 1.24 – 1.12 (m, 40H), 0.77 (dt, *J* = 21.0, 7.0 Hz, 12H).

^{13}C-NMR (151 MHz, $C_2D_2Cl_4$): δ 167.2, 166.2, 128.6, 128.0, 127.9 127.6, 125.7, 125.6, 124.6, 123.8, 123.0, 122.1, 122.0, 121.4, 32.2, 30.0, 29.9, 29.8, 29.7, 29.2, 29.0, 26.5, 23.0, 14.5

HR-MS (MALDI-ToF): m/z ($[M]^+$) = 1240.7471, calcd. for $C_{82}H_{100}N_2O_8$: m/z = 1240.7479, error = -0.7 ppm.

IR: $\tilde{\nu}$ = 2921, 2853, 1713, 1195, 1128, 747 cm^{-1}

The ^{1}H-NMR spectra of **DU-1** showed broad signals in the aromatic region at room temperature. After the addition of the reducing agent hydrazine to quench radical impurities, sharp signals were observed in NMR spectra in tetrachloroethane. Due to the presence of water and hydrazine, the integration of the alkyl chains is disturbed. Furthermore, the ^{13}C-NMR spectrum is complex due to different conformations of the alkyl chains. Due to the low solubility in d_2-tetrachloroethane, chemical shifts of ^{13}-C nuclei were derived from the HSQC or from HMBC experiments. Unfortunately, not all quaternary carbon atoms could be detected.

Tetradodecylbenzo[7',8']indolizino[6',5',4',3':8,1,2]isoquinolino[4,3-*j*]benzo[7,8]indolizino[6,5,4,3-*def*]phenanthridine-1,2,11,12-tetracarboxylate (**DU-2**)

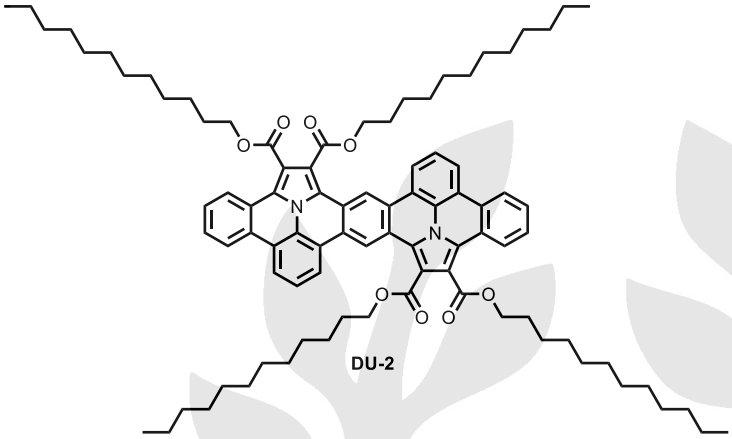

DU-2: R_f = 0.3 (SiO_2; DCM). Mp: 206.5 °C. Yield = 61% over 2 steps.

^{1}H-NMR (600 MHz, $C_2D_2Cl_4$): 9.54 (s, 2H), 8.10 (d, *J* = 7.5 Hz, 2H), 8.04 (d, *J* = 7.6 Hz, 2H), 7.85 (d, *J* = 7.3 Hz, 2H), 7.72 (d, *J* = 7.2 Hz, 2H), 7.47 (t, *J* = 7.2 Hz, 2H), 7.21 (t, *J* = 7.0 Hz, 2H), 7.10 (t, *J* = 6.5 Hz, 2H), 4.48 – 4.40 (m, 7H), 4.40 – 4.27 (m, 8H), 1.79 (d, *J* = 6.8 Hz, 8H), 1.42 (d, *J* = 6.1 Hz, 8H), 1.37 – 1.25 (m, 8H), 1.12 (dd, *J* = 28.9, 25.8 Hz, 60H), 0.72 (dd, *J* = 16.3, 6.8 Hz, 12H).

^{13}C-NMR (151 MHz, $C_2D_2Cl_4$): δ 167.54, 166.39, 128.55, 127.94, 127.87, 126.50, 126.22, 125.64, 124.50, 124.07, 123.80, 123.42, 122.26, 122.20, 122.03, 121.32, 120.57, 120.07, 74.20, 32.20, 30.02, 30.00, 29.98, 29.93, 29.80, 29.67, 29.16, 29.03, 26.55, 26.52, 23.00, 14.51, 14.50.

HR-MS (MALDI-ToF): m/z ($[M]^+$) = 1352.8741, calcd. for $C_{90}H_{116}N_2O_8$: m/z = 1352.8731, error = 0.7 ppm

IR: $\tilde{\nu}$ = 2918, 2851, 1713, 1194, 1126, 747 cm^{-1}.

The ^{1}H-NMR spectra of **DU-2** showed broad signals in the aromatic region at room temperature. After the addition of the reducing agent hydrazine to quench radical impurities, sharp signals were observed in NMR spectra in tetrachloroethane. Due to the presence of water and hydrazine, the integration of the alkyl chains is disturbed. Furthermore, the ^{13}C-NMR spectrum is complex due to different conformations of the alkyl chains. Due to the low solubility in d_2-tetrachloroethane, not all quaternary carbon atoms could be detected.

Tetranonaylbenzo[7',8']indolizino[6',5',4',3':8,1,2]isoquinolino[4,3-*j*]benzo[7,8]indolizino[6,5,4,3-*def*]phenanthridine-1,2,11,12-tetracarboxylate (**DU-3**)

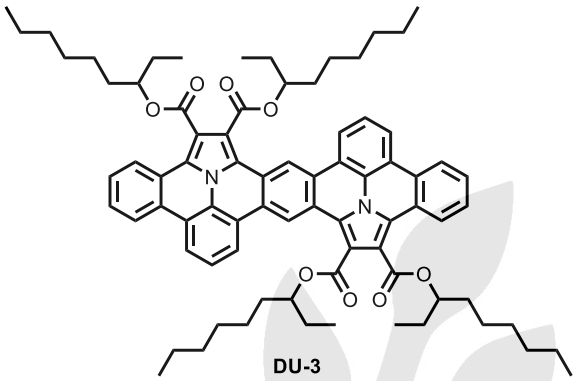

DU-3: R_f = 0.5 (SiO_2; DCM). Mp: 203.8 °C. Yield = 61% over 2 steps.

^{1}H-NMR (600 MHz, $C_2D_2Cl_4$): δ 9.78 (s, 2H), 8.39 (dd, *J* = 24.5, 6.4 Hz, 4H), 8.24 (d, *J* = 6.7 Hz, 2H), 8.16 (s, 2H), 7.69 (t, *J* = 7.5 Hz, 2H), 7.42 (s, 4H), 5.28 – 5.21 (m, 2H), 5.17 – 5.04 (m, 2H), 1.86 – 1.61 (m, 20H), 1.34 (d, *J* = 37.1 Hz, 12H), 1.26 – 1.14 (m, 12H), 1.08 (d, *J* = 2.8 Hz, 8H), 1.01 – 0.89 (m, 12H), 0.81 (d, *J* = 1.1 Hz, 6H), 0.66 (d, *J* = 6.2 Hz, 6H).

^{13}C-NMR (151 MHz, $C_2D_2Cl_4$): δ 166.84, 166.79, 128.82, 128.68, 128.17, 127.11, 126.64, 126.62, 125.73, 125.72, 125.26, 125.24, 125.22, 124.67, 124.24, 124.14, 123.78, 123.27, 123.25, 122.87, 122.31, 122.29, 121.77, 120.13, 120.10, 116.85, 114.87, 114.38, 114.35, 74.20, 33.56, 33.46, 32.91, 32.11, 32.00, 29.80, 29.67, 26.83, 26.17, 25.72, 25.51, 22.98, 22.89, 14.51, 14.37, 10.06, 9.82.

HR-MS (MALDI-ToF): m/z ($[M]^+$) = 1184.6855, calcd. for $C_{78}H_{92}N_2O_8$: m/z = 1184.6853, error = 0.1 ppm.

IR: $\tilde{\nu}$ = 2954, 2924, 2858, 1703, 1194, 744 cm^{-1}.

The ^{1}H-NMR spectra of **DU-3** showed broad signals in the aromatic region at room temperature. After the addition of the reducing agent hydrazine to quench radical impurities, sharp signals were observed in NMR spectra in tetrachloroethane. Due to the presence of water and hydrazine, the integration of the alkyl chains is disturbed. Furthermore, the ^{13}C-NMR spectrum is complex due to different conformations of the alkyl chains.

3) UV-Vis Absorption Spectroscopy

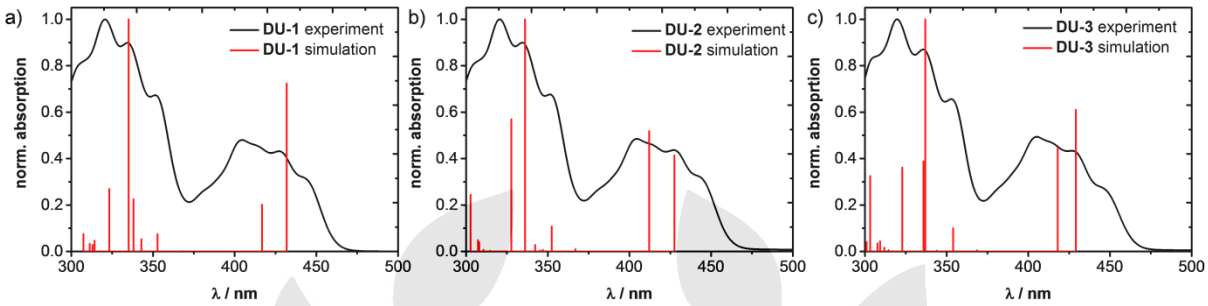

Figure S1. (a) UV-Vis absorption spectra of **DU-1** in DCM (black line: experiment; red line: simulation based on DFT calculations). (b) UV-Vis absorption spectra of **DU-2** in DCM (black line: experiment; red line: simulation based on DFT calculations). (c) UV-Vis absorption spectra of **DU-3** in DCM (black line: experiment; red line: simulation based on DFT calculations).

Table S1. Summarized results of the simulated absorption spectrum of **DU-1**.

Excited State	Energy [eV]	Wavelength [nm]	Oscillator Strength	Configurations
1	2.87	431	0.6708	HOMO → LUMO 0.65502
2	2.98	416	0.1866	HOMO → LUMO+1 0.63158
5	3.52	352	0.0695	HOMO → LUMO+3 0.46258
				HOMO → LUMO+4 0.44486
7	3.62	343	0.0489	HOMO-2 → LUMO 0.44909
				HOMO → LUMO+3 0.32185
8	3.67	338	0.2085	HOMO-2 → LUMO 0.44669
				HOMO → LUMO+4 0.32177
9	3.70	335	0.9269	HOMO-2 → LUMO+1 0.67095
10	3.84	323	0.2502	HOMO → LUMO+5 0.57090

Table S2. Summarized results of simulated absorption spectrum of **DU-2**.

Excited State	Energy [eV]	Wavelength [nm]	Oscillator Strength	Configurations
1	2.90	427	0.3785	HOMO → LUMO 0.66140
2	3.01	412	0.4743	HOMO → LUMO+1 0.65817
4	3.52	352	0.0988	HOMO → LUMO+3 0.52741
8	3.62	342	0.0260	HOMO → LUMO+4 0.51956
				HOMO → LUMO+5 0.36420
9	3.69	336	0.9149	HOMO-2 → LUMO 0.65461
10	3.79	327	0.5210	HOMO-2 → LUMO+1 0.60816

Table S3. Summarized results of simulated absorption spectrum of **DU-3**.

Excited State	Energy [eV]	Wavelength [nm]	Oscillator Strength	Configurations
1	2.89	429	0.4909	HOMO → LUMO 0.68879
2	2.97	418	0.3600	HOMO → LUMO+1 0.67639
4	3.50	354	0.0807	HOMO → LUMO+3 0.45748
				HOMO → LUMO+4 0.46417
8	3.68	337	0.8046	HOMO-2 → LUMO 0.48869
9	3.69	336	0.3125	HOMO-2 → LUMO 0.40439
				HOMO-2 → LUMO+1 0.42064
10	3.84	323	0.2908	HOMO → LUMO+5 0.54918

4) Fluorescence Emission Spectroscopy

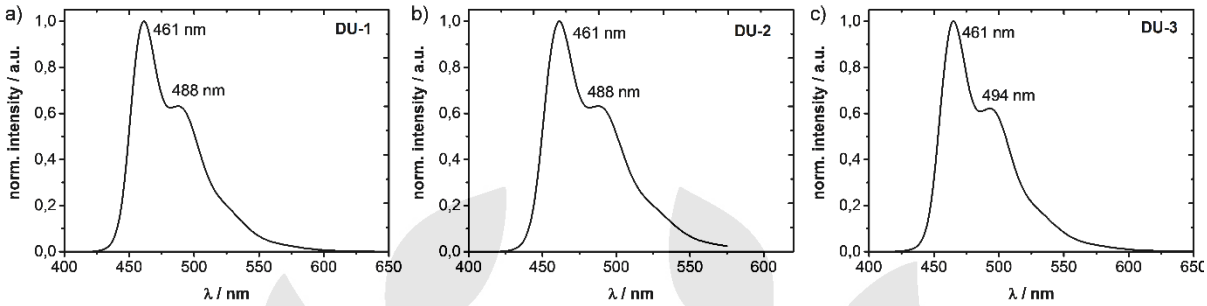

Figure S2. (a) Fluorescence emission spectrum of **DU-1** in DCM. (b) Fluorescence emission spectrum of **DU-2** in DCM. (c) Fluorescence emission spectrum of **DU-3** in DCM.

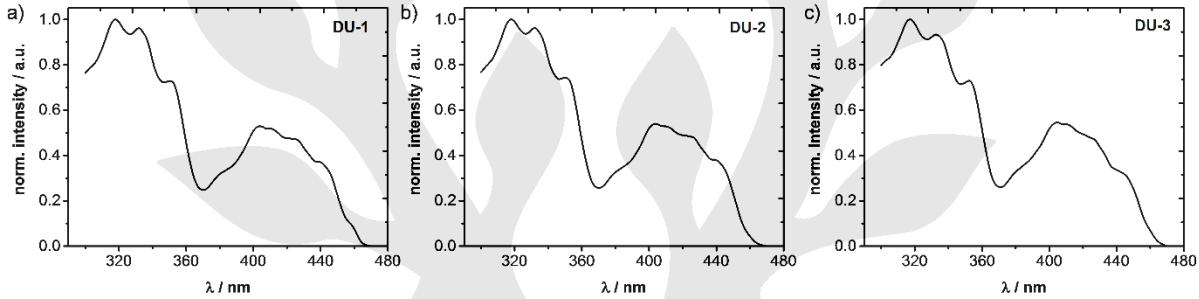

Figure S3. (a) Fluorescence excitation spectrum of **DU-1** in DCM. (b) Fluorescence excitation spectrum of **DU-2** in DCM. (c) Fluorescence excitation spectrum of **DU-3** in DCM.

5) Cyclic Voltammetry

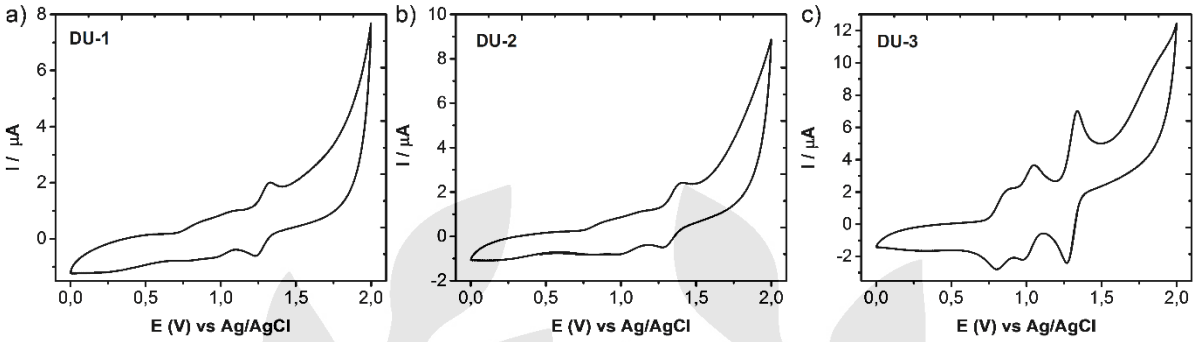

Figure S4. (a) Cyclic voltammetry of **DU-1** in DCM. (b) Cyclic voltammetry of **DU-2** in DCM. (c) Cyclic voltammetry of **DU-3** in DCM.

6) Differential Scanning Calorimetry (DSC)

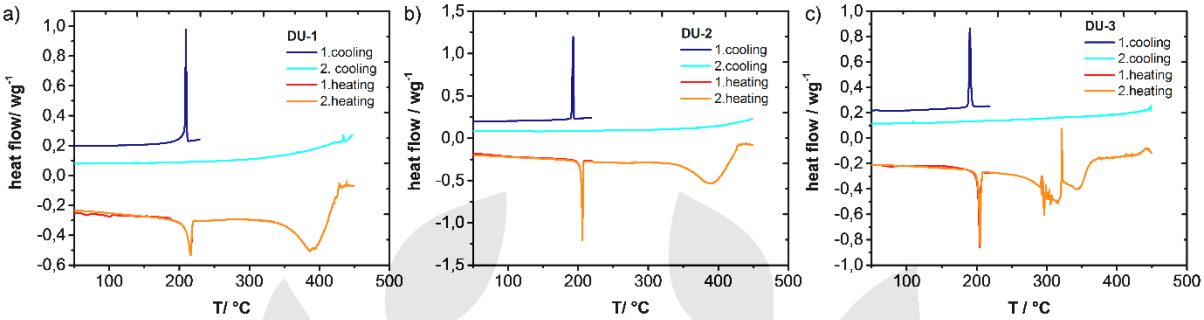

Figure S5. DSC measurements of (a) **DU-1**, (b) **DU-2** and (c) **DU-3** with first and second heating as well as first and second cooling scan.

7) Thermogravimetric Analysis

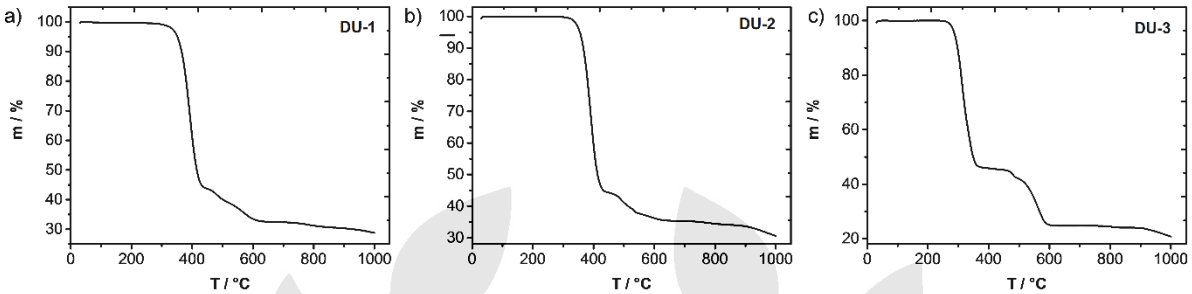

Figure S5. (a) TGA measurements of **DU-1**. (b) TGA measurements of **DU-2**. (c) TGA measurements of **DU-3**.

8) Infrared Spectroscopy

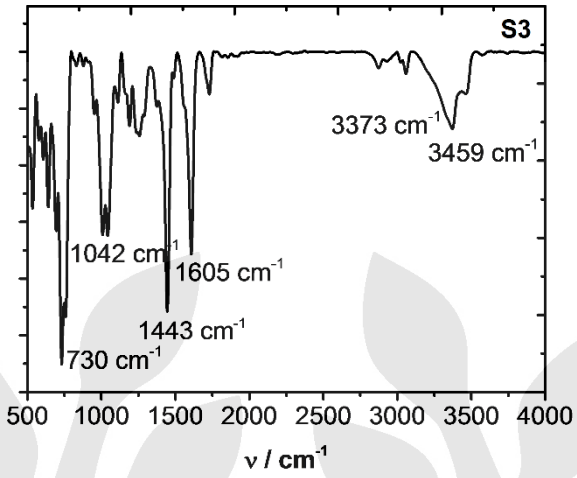

Figure S6. IR spectrum of **S3**.

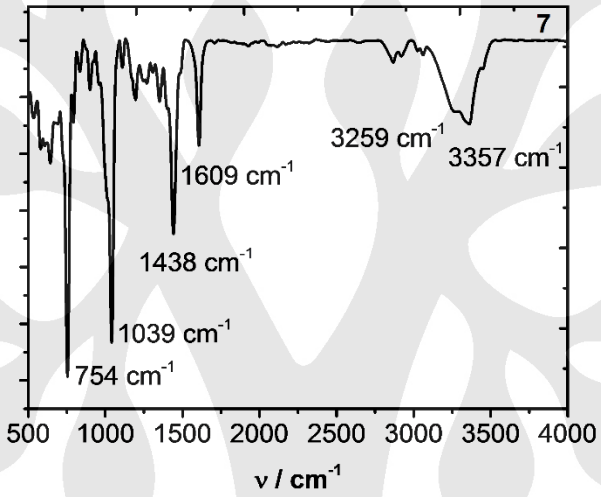

Figure S7. IR spectrum of **7**

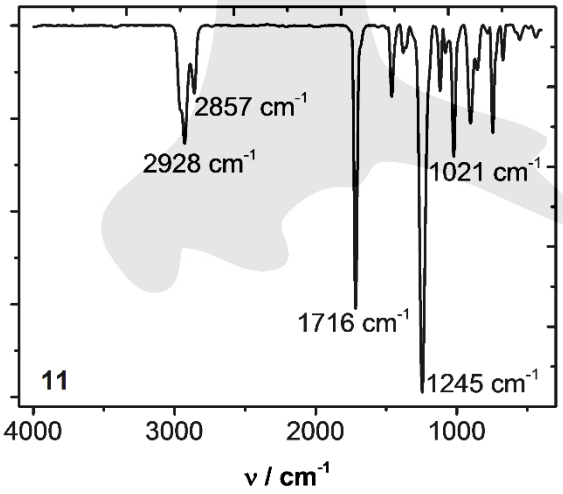

Figure S8. IR spectrum of **11**.

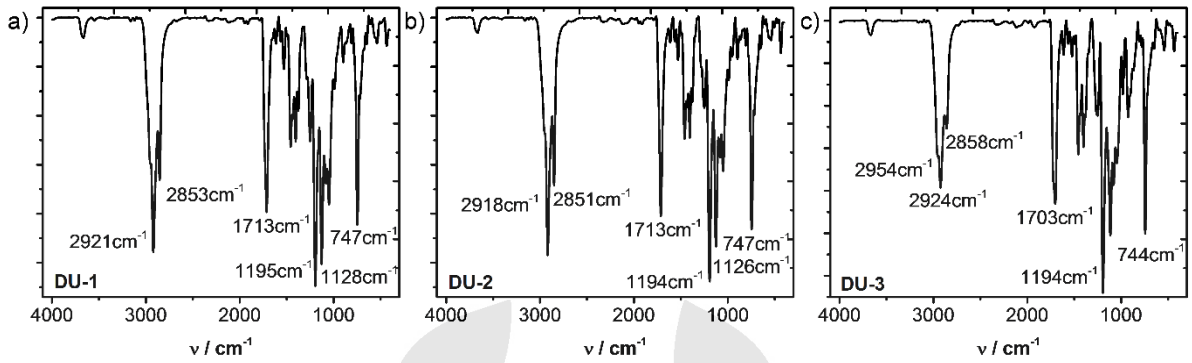

Figure S9. (a) IR spectrum of **DU-1**. (b) IR spectrum of **DU-2**. (c) IR spectrum of **DU-3**.

9) DFT Calculations

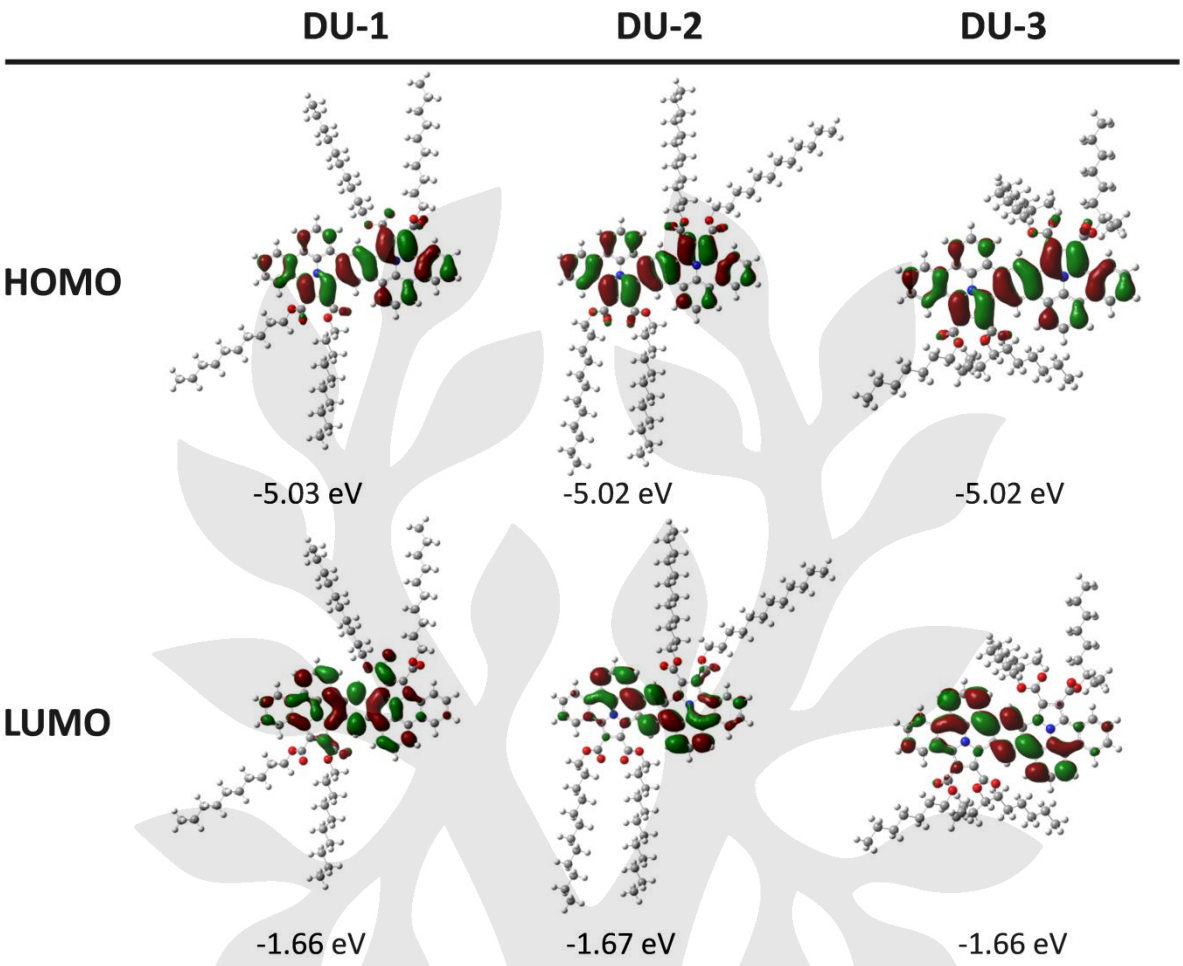

Figure S10. Quantum-chemical DFT calculations of **DU-1-3** with a B3LYP functional and 6-31G(d) basis set (HOMO level: top; LUMO level: down).

10) Summary of the Optoelectronic Properties

Table S4. Comparison of the experimental and calculated values of the electronic properties

	UV-Vis absorption		photo-luminescence		electrochemistry		DFT calculations		
	Λ_{abs}[a] [nm]	$E_g^{opt,b}$ [eV]	$\Lambda_{em,max}$[c] [nm]	Φ[d] [%]	E_{HOMO}[e] [eV]	E_{LUMO}[f] [eV]	E_{HOMO}[g] [eV]	E_{LUMO}[g] [eV]	$\Delta E_g^{DFT,h}$ [eV]
DU-1	427	2.67	461	37.6	-5.07	-2.40	-5.03	-1.66	3.37
DU-2	427	2.67	461	32.9	-5.08	-2.41	-5.02	-1.67	3.35
DU-3	427	2.67	464	37.7	-5.10	-2.43	-5.02	-1.66	3.36

[a] Absorption at maximum wavelength. [b] Optical energy gap calculated from the UV/vis absorption maxima using the Planck-Einstein relation. [c] Emission at maximum wavelength. [d] Quantum yields were measured from integrating-sphere method.[1] [e] E_{HOMO} estimated from the onset potential of the first oxidation wave. [f] E_{LUMO} was estimated according to $E_{LUMO} = E_{HOMO} + \Delta Eg^{opt}$. [g] E_{HOMO} and E_{LUMO} level calculated by DFT Gaussian 09 package. [h] Energy gap calculated according to $\Delta E_g^{DFT}=E_{HOMO}-E_{LUMO}$.

11) X-Ray Diffraction

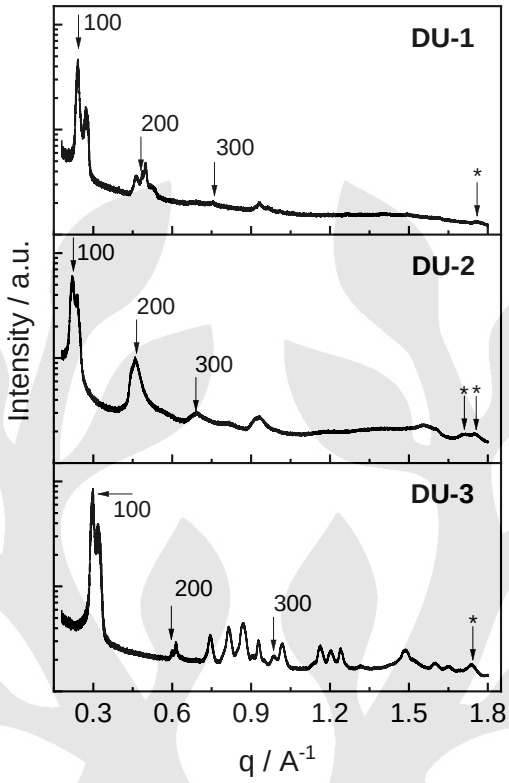

Figure S12. X-Ray diffraction spectra of **DU-1**, **DU-2** and **DU-3**. Numbers in the 1D integration denote the peaks corresponding to h00 Bragg series of DU derivatives. The π-stacking interaction has been marked by *.

12) High-Resolution Mass Spectroscopy

12.1.) High-Resolution Atmospheric Pressure Chemical Ionization Mass Spectroscopy (HR-APCI-MS)

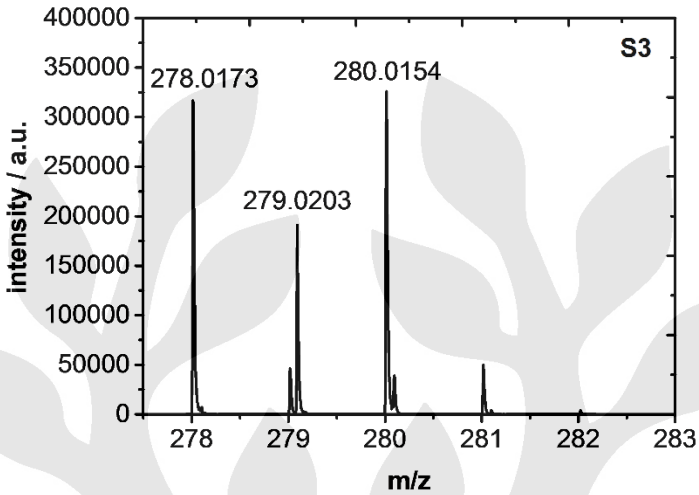

Figure S11. HR-APCI spectrum of **S3.**

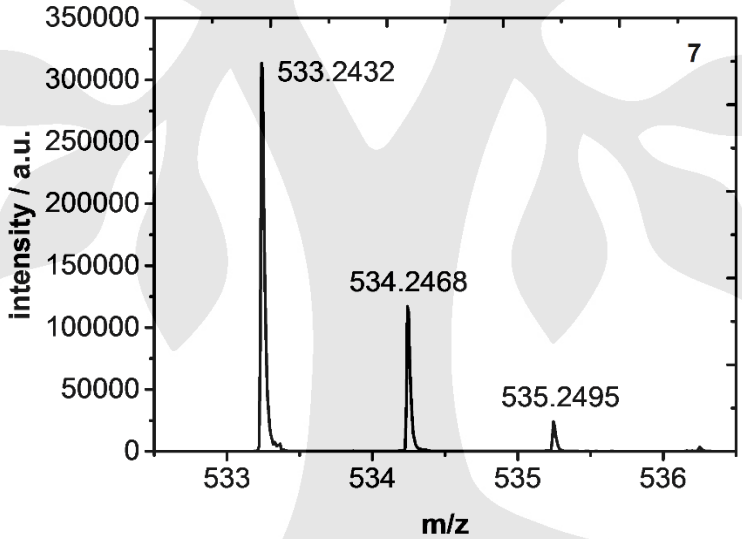

Figure S12. HR-APCI spectrum of **7.**

12.2.) High-Resolution Matrix Assisted Laser Desorption/Ionization Time of Flight Mass Spectroscopy (HR-MALDI-TOF-MS)

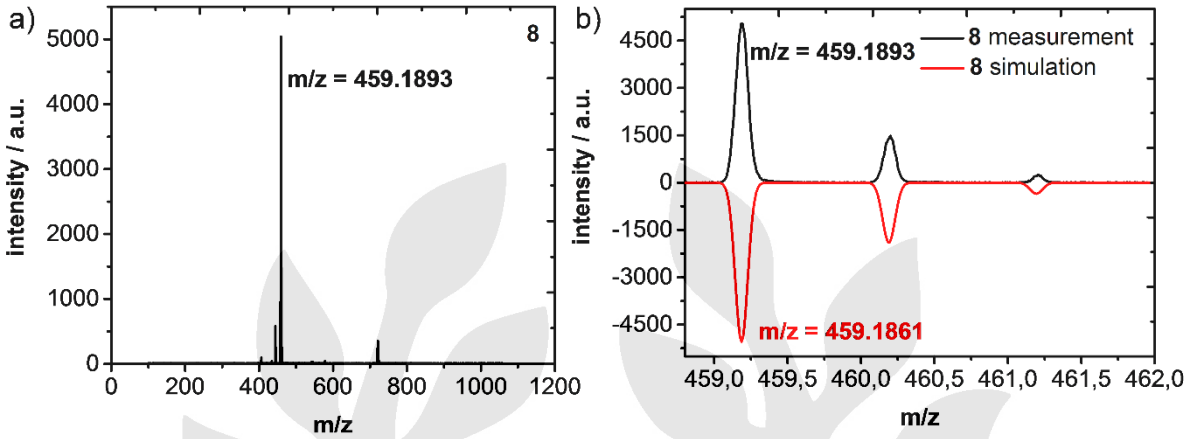

Figure S13. (a) HR-MALDI-TOF spectrum of **8**. (b) HR-MALDI-TOF measurement of **8** (black line) is in agreement with the expected isotopic distribution pattern (red line).

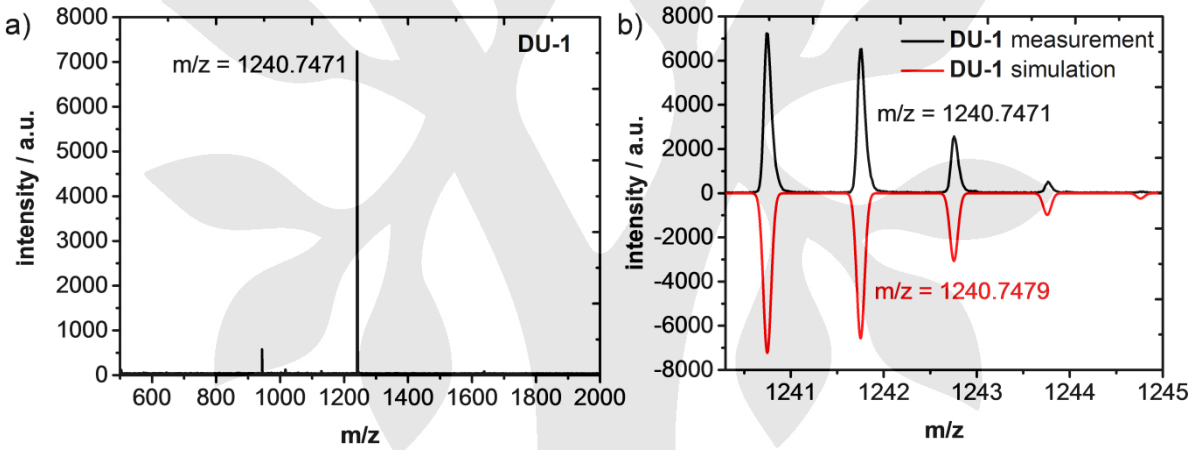

Figure S14. (a) HR-MALDI-TOF spectrum of **DU-1**. (b) HR-MALDI-TOF measurement of **DU-1** (black line) is in agreement with the expected isotopic distribution pattern (red line).

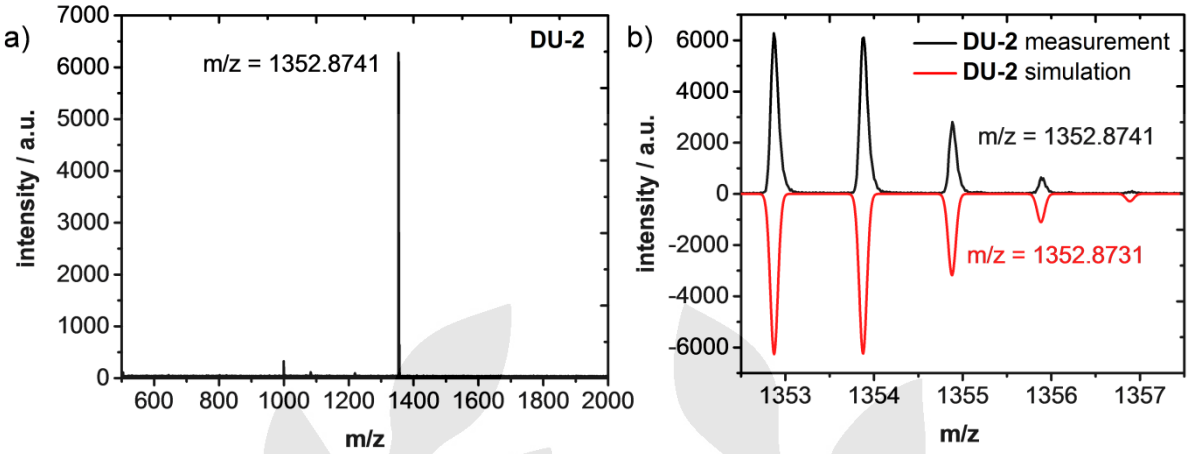

Figure S15. (a) HR-MALDI-TOF spectrum of **DU-2**. (b) HR-MALDI-TOF measurement of **DU-2** (black line) is in agreement with the expected isotopic distribution pattern (red line).

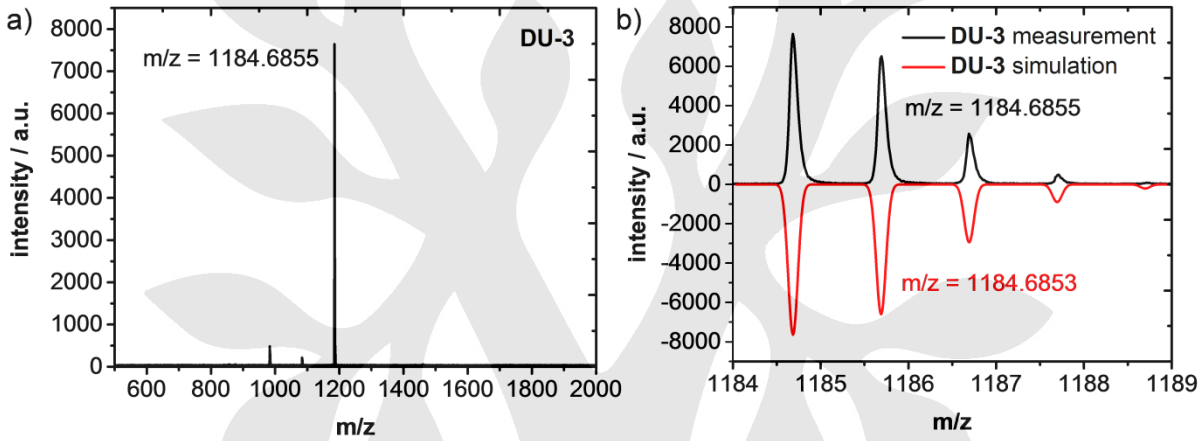

Figure S16. (a) HR-MALDI-TOF spectrum of **DU-3**. (b) HR-MALDI-TOF measurement of **DU-3** (black line) is in agreement with the expected isotopic distribution pattern (red line).

13) Nuclear Magnetic Resonance Spectroscopy

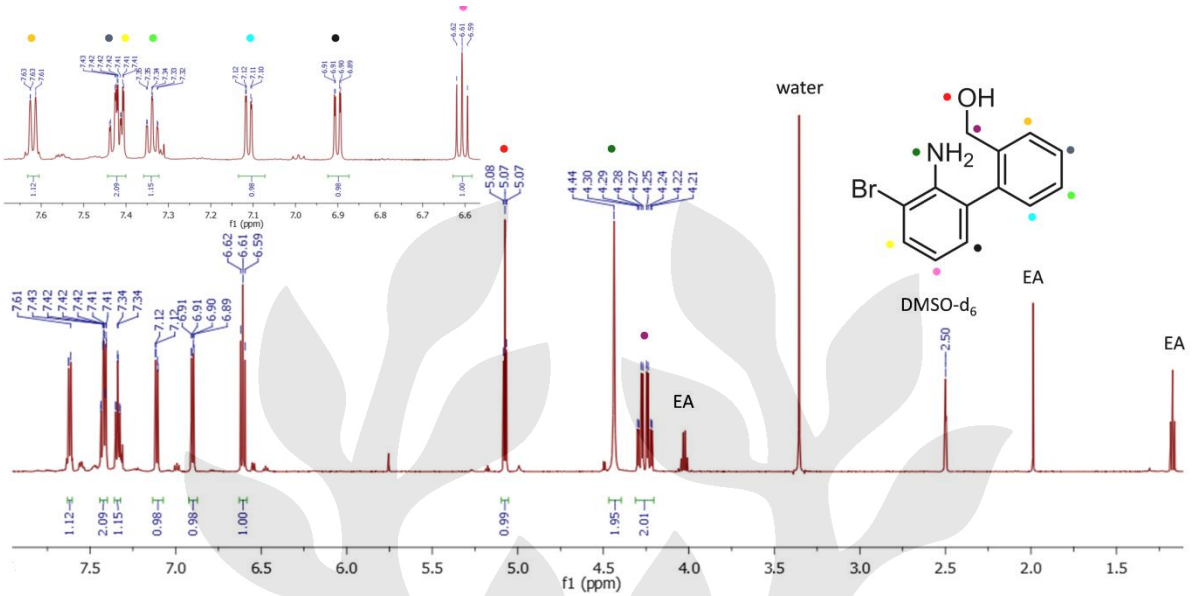

Figure S17. ^{1}H-NMR (600 MHz) spectrum of compound **S3** at 298 K in DMSO-d_6.

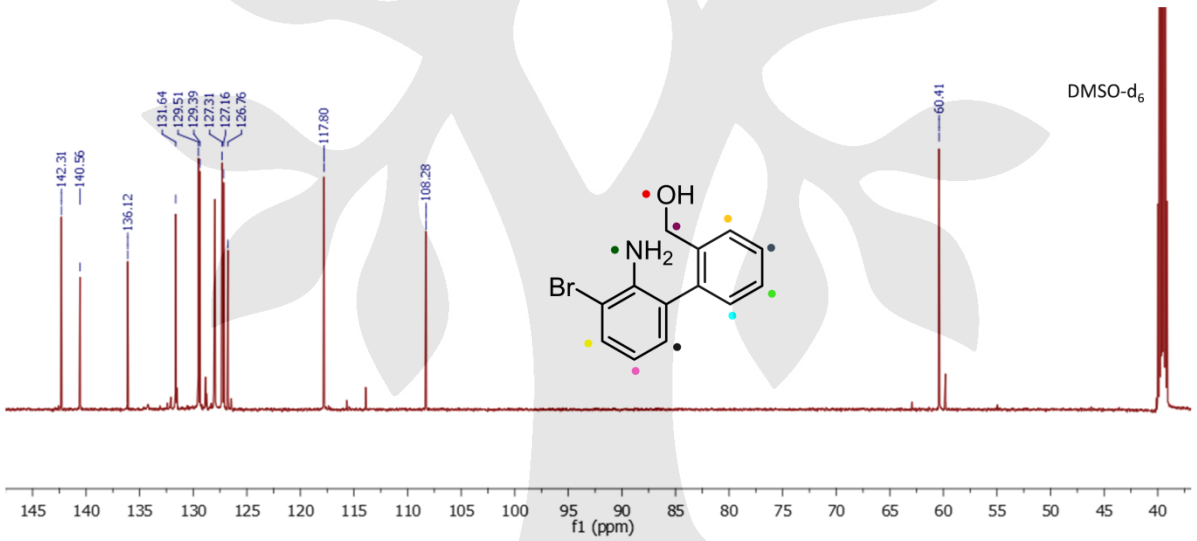

Figure S18. ^{13}C-NMR (151 MHz) spectrum of compound **S3** at 298 K in DMSO-d_6.

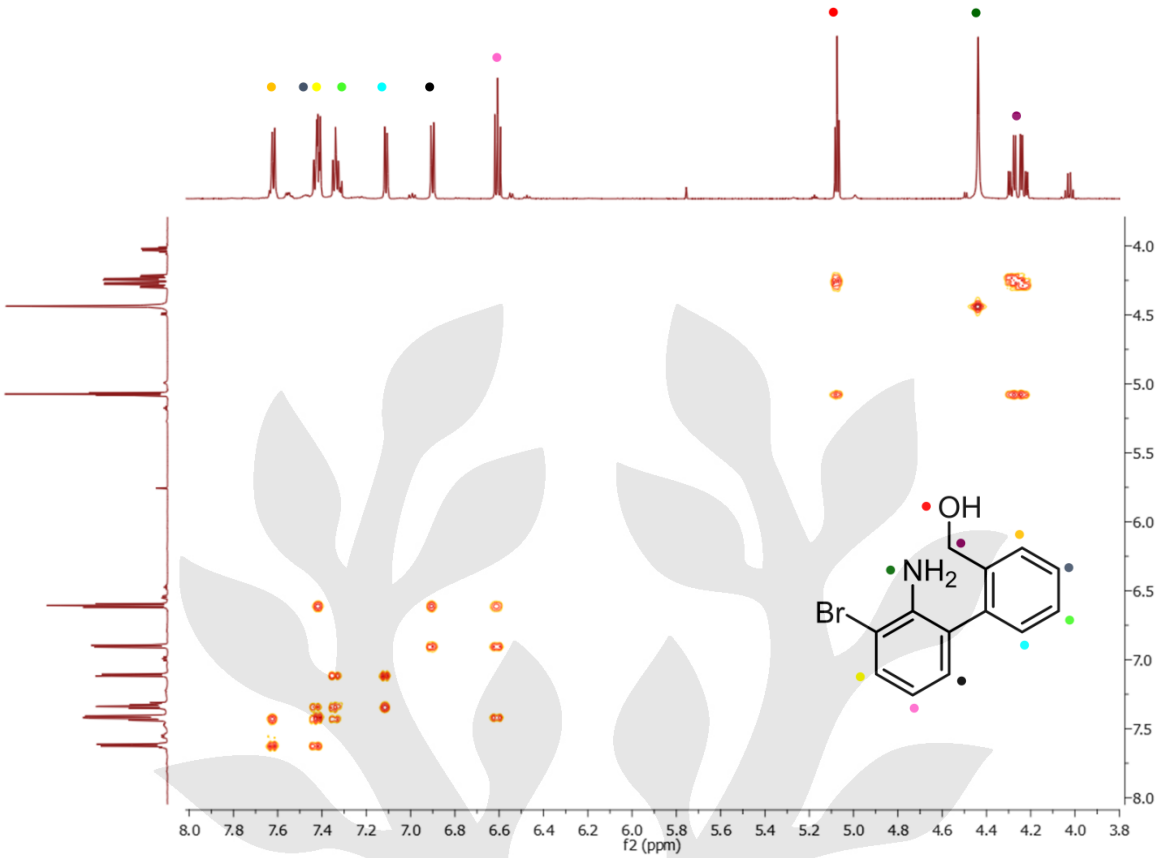

Figure S19. Correlation spectrum (COSY) of **S3** at 298 K in DMSO-d_6.

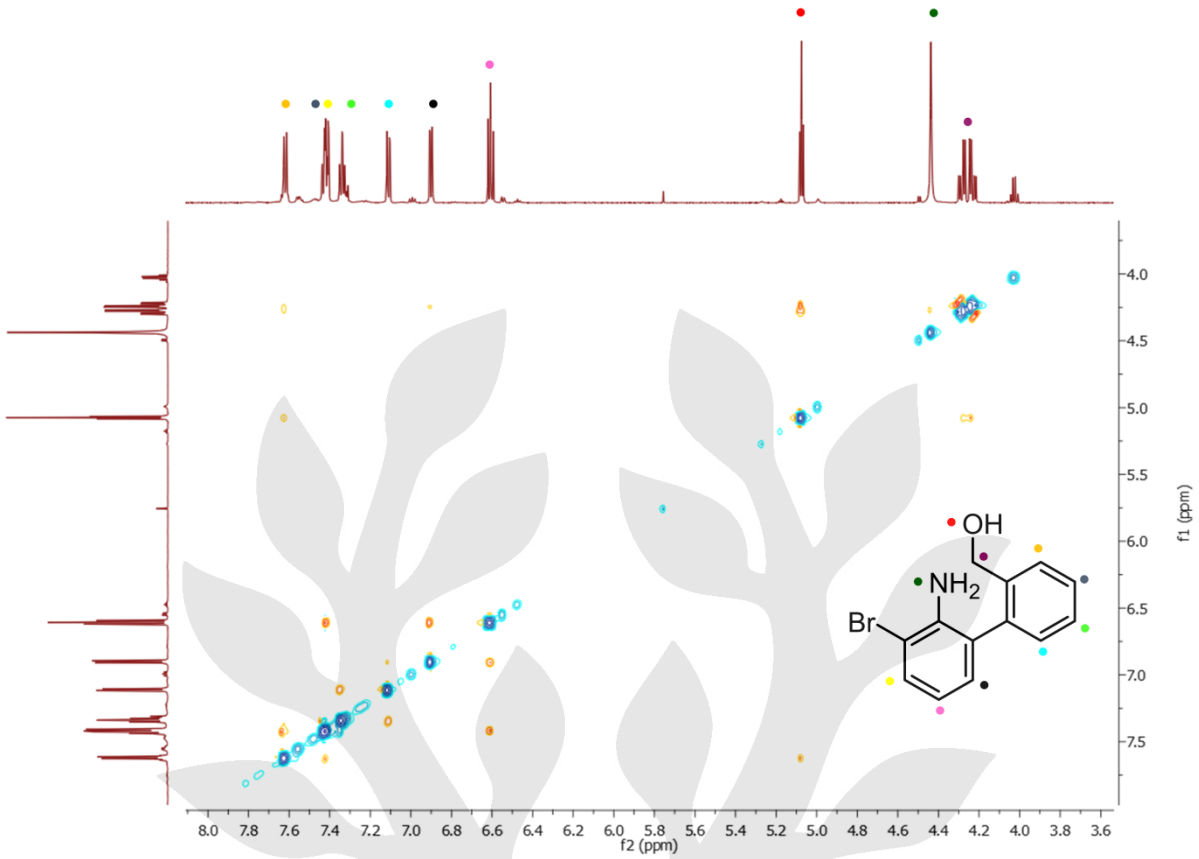

Figure S20. Nuclear Overhauser effect spectrum (NOESY) for **S3** at 298 K in DMSO-d_6.

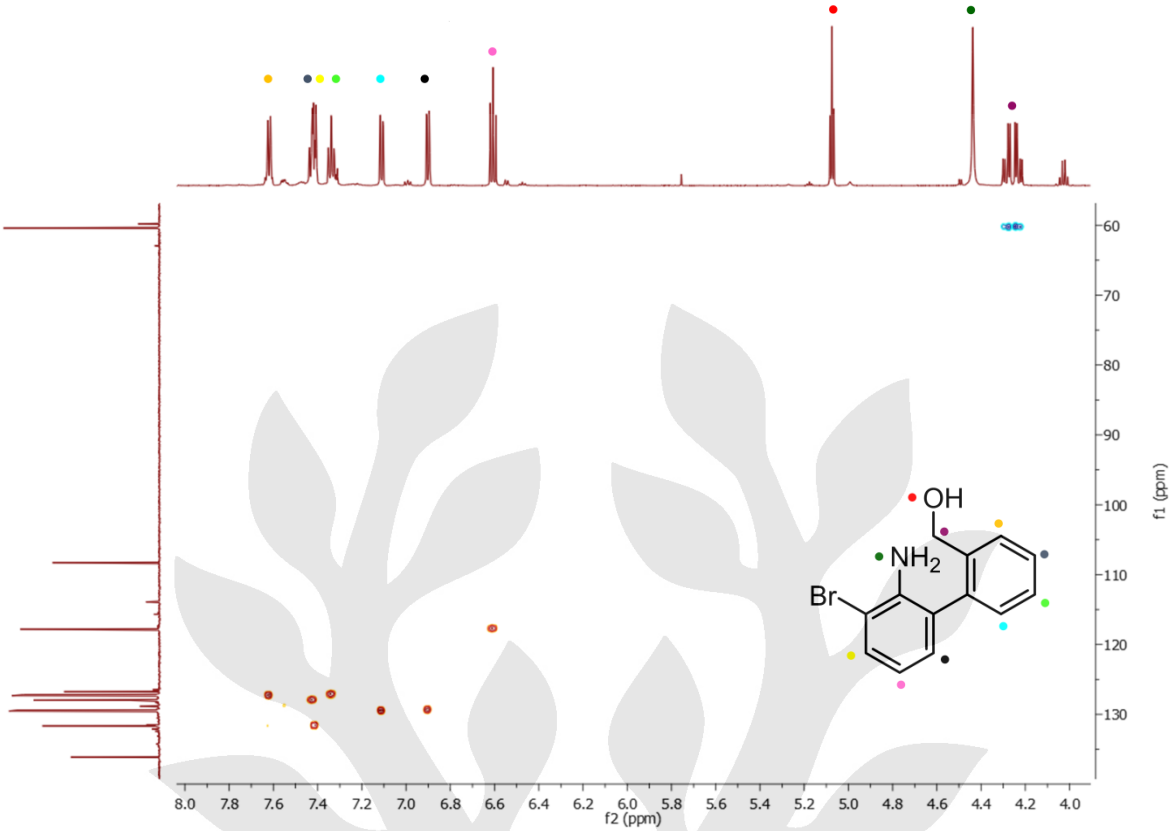

Figure S21. Heteronuclear single quantum coherence (HSQC) spectrum for **S3** at 298 K in DMSO-d_6.

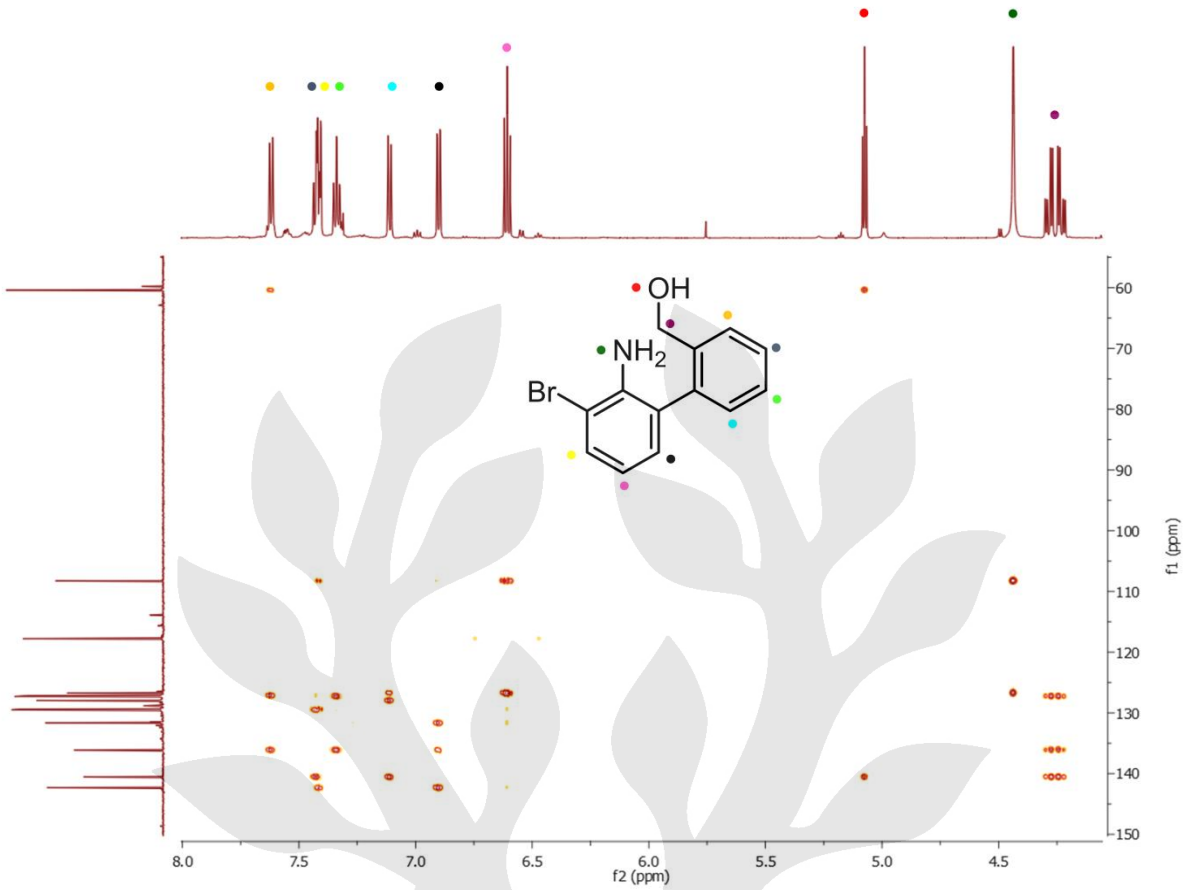

Figure S22. Heteronuclear multiple-bond correlation (HMBC) spectrum for **S3** at 298 K in DMSO-d_6.

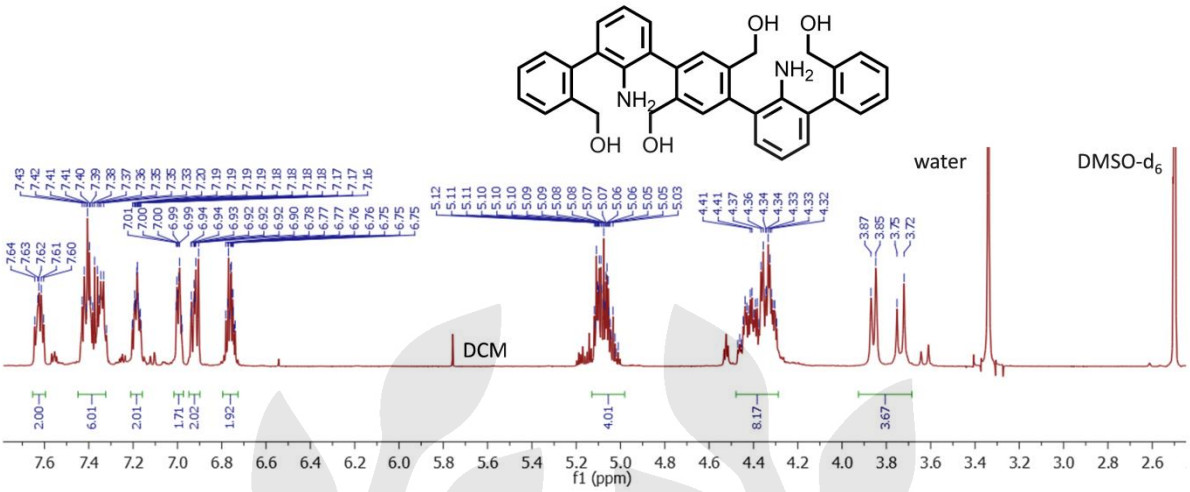

Figure S23. ^{1}H-NMR (600 MHz) spectrum of compound **7** at 298 K in DMSO-d_6.

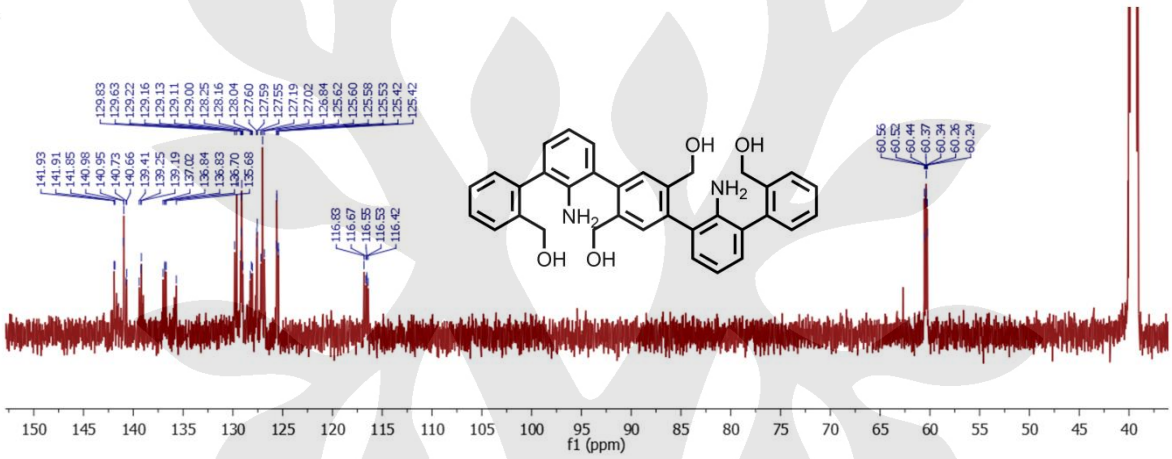

Figure S24. ^{13}C-NMR (151 MHz) spectrum of compound **7** at 298 K in DMSO-d_6.

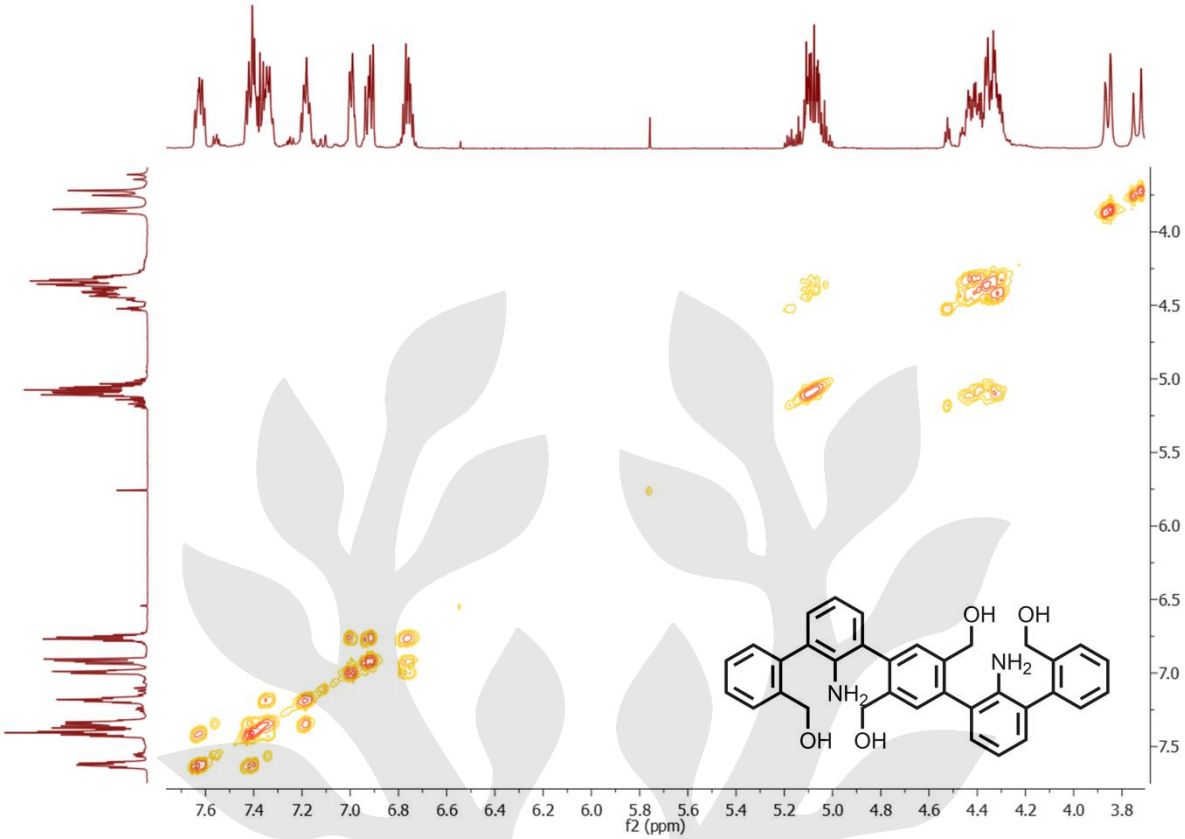

Figure S25. Correlation spectrum (COSY) of **7** at 298 K in DMSO-d_6.

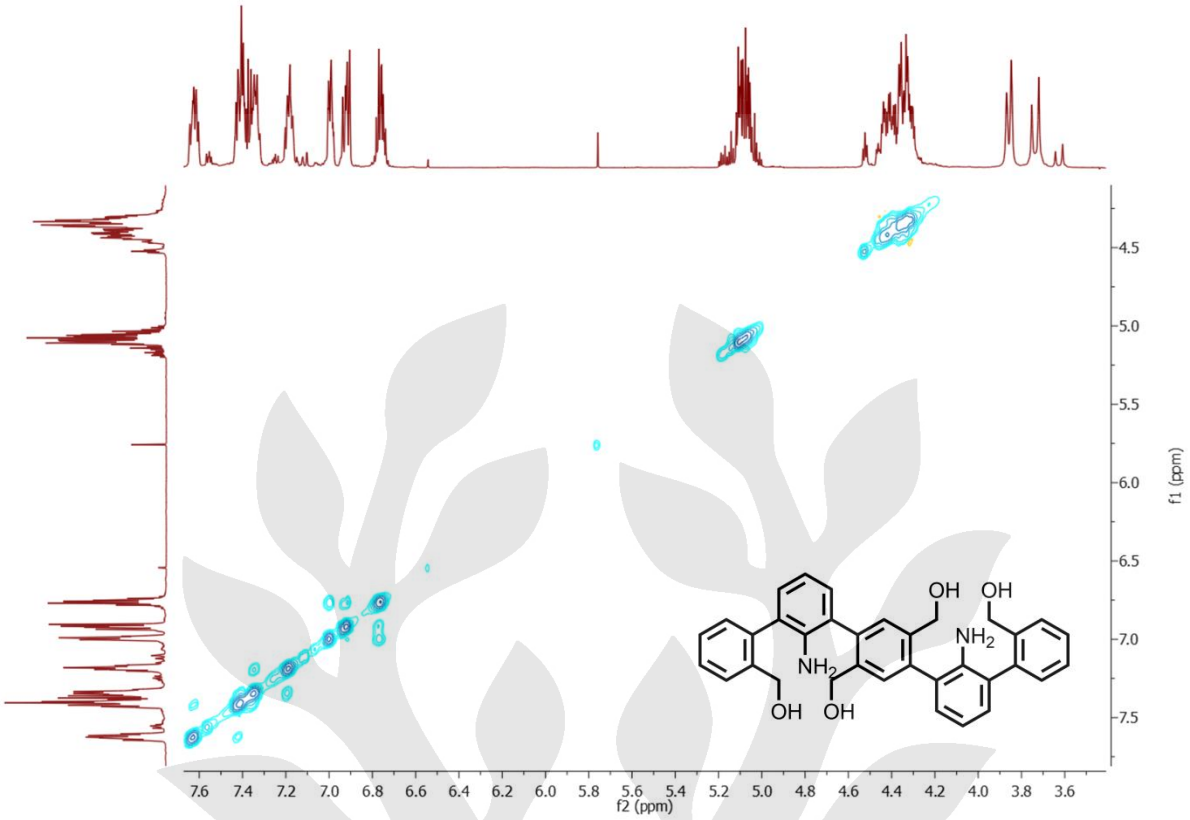

Figure S26. Nuclear Overhauser effect spectrum (NOESY) for **7** at 298 K in DMSO-d_6.

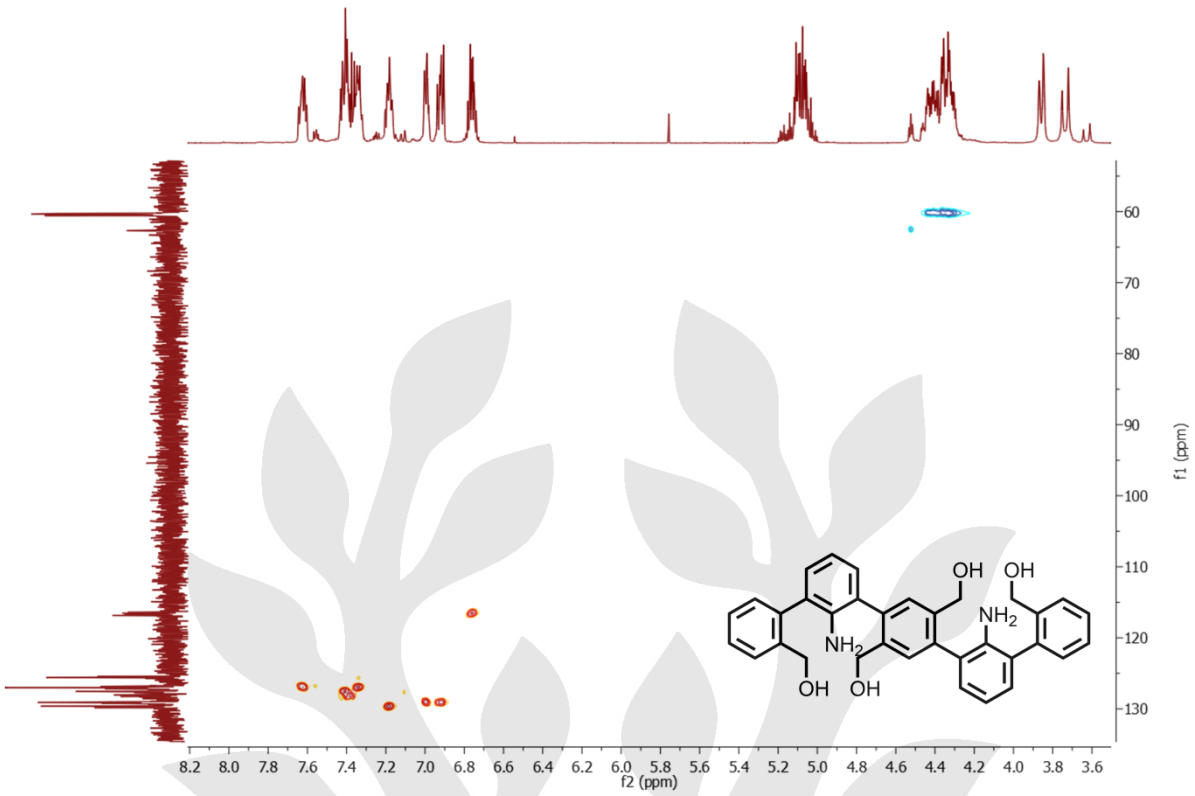

Figure S27. Heteronuclear single quantum coherence (HSQC) spectrum for **7** at 298 K in DMSO-d_6.

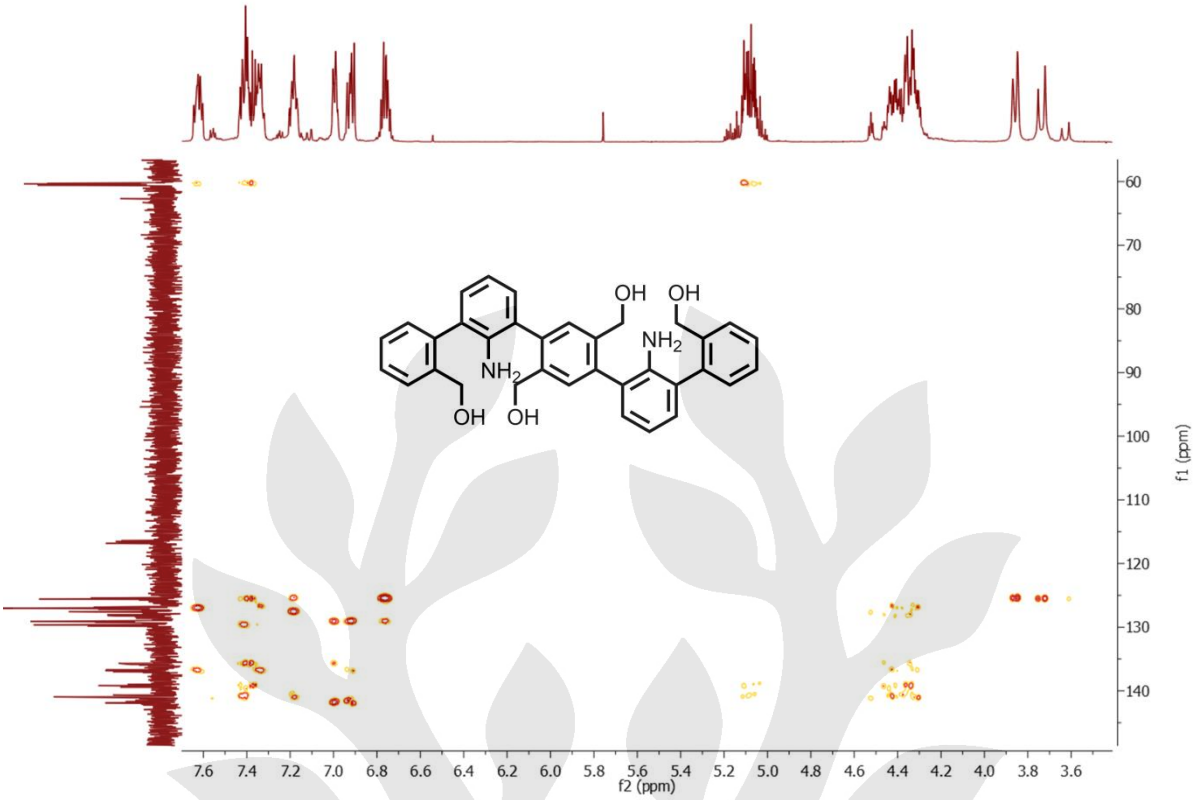

Figure S28. Heteronuclear multiple-bond correlation (HMBC) spectrum for **7** at 298 K in DMSO-d_6

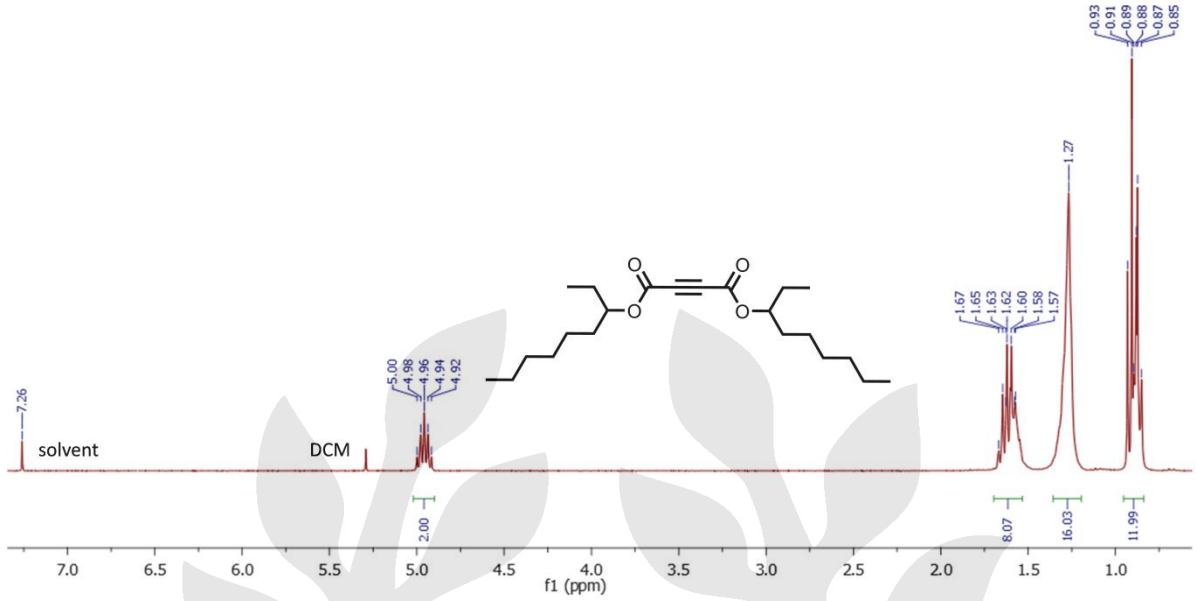

Figure S29. ^{1}H-NMR (600 MHz) spectrum of compound **11** at 298 K in $CDCl_3$.

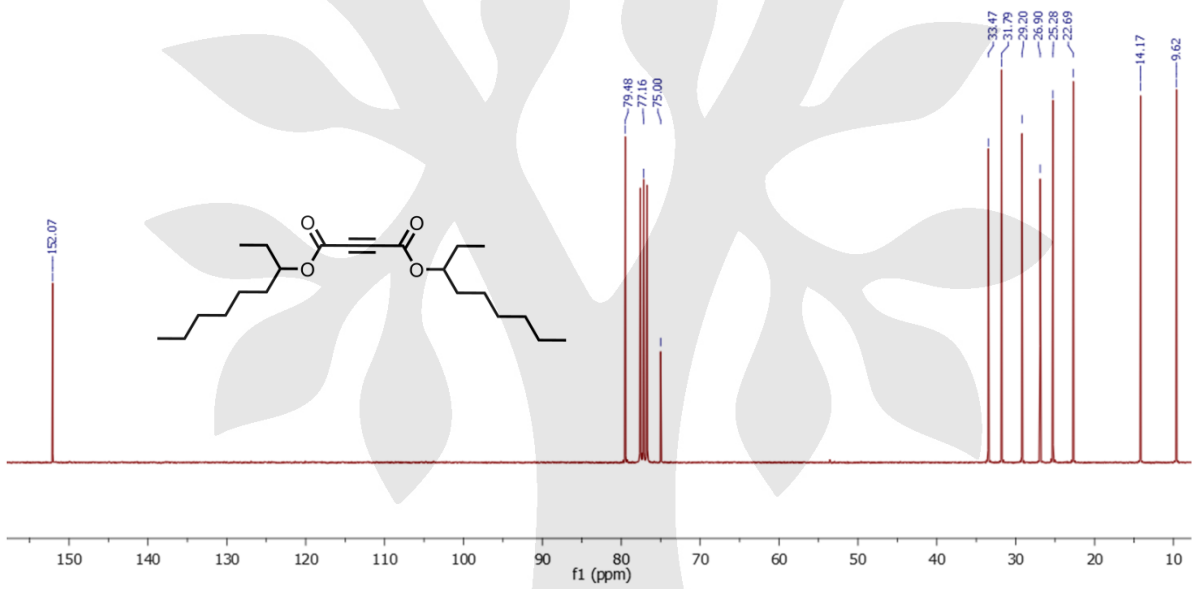

Figure S30. ^{13}C-NMR (151 MHz) spectrum of compound **11** at 298 K in $CDCl_3$.

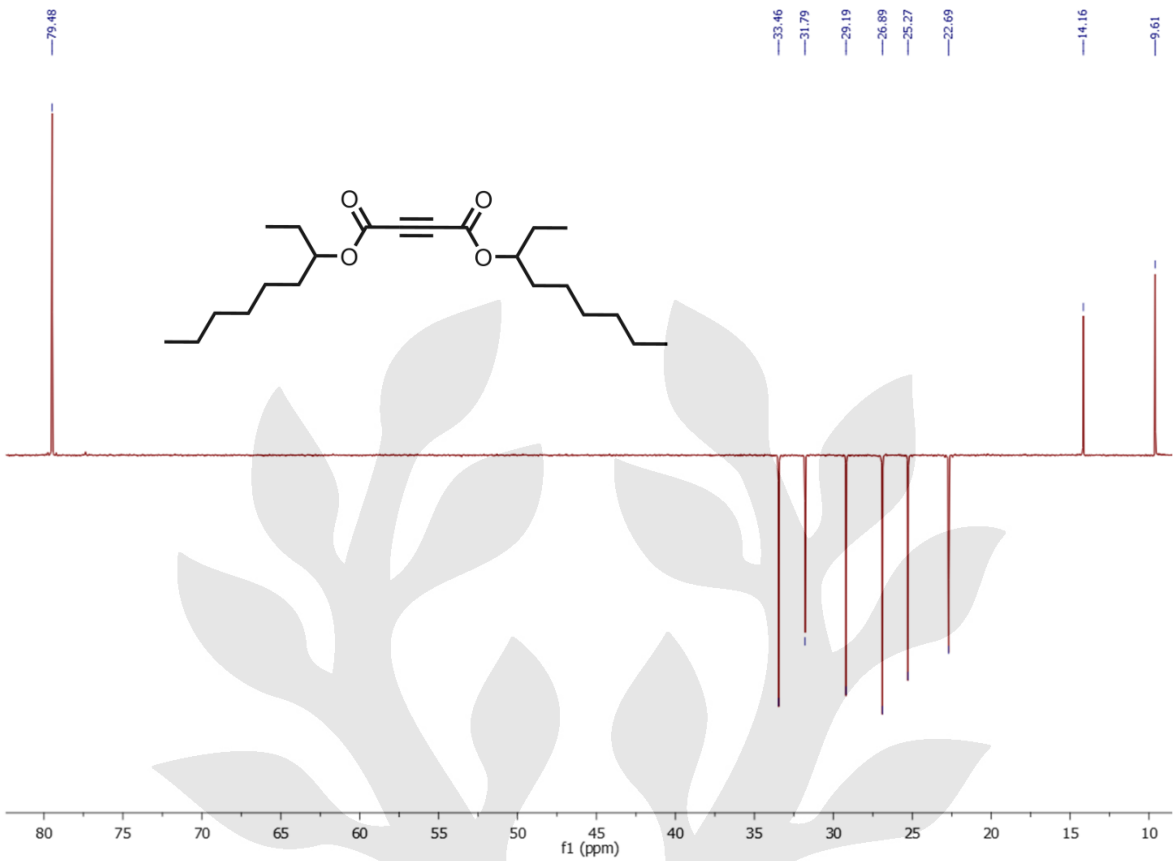

Figure S31. ^{13}C-Distortionless Enhancement by Polarization Transfer (DEPT)-NMR (151 MHz) spectrum of compound **11** at 298 K in $CDCl_3$.

The ^{1}H-NMR spectra of **DU-1-3** showed broad signals at room temperature. After the addition of the reducing agent hydrazine to quench radical impurities, sharp signals were observed in NMR spectra in $C_2D_2Cl_4$. The ^{13}C- and 2D-NMR spectra (correlation spectroscopy (COSY), heteronuclear single quantum coherence (HSQC), heteronuclear multiple-bond correlation (HMBC) and nuclear Overhauser effect epectroscopy (NOESY)) were further measured after addition of hydrazine.

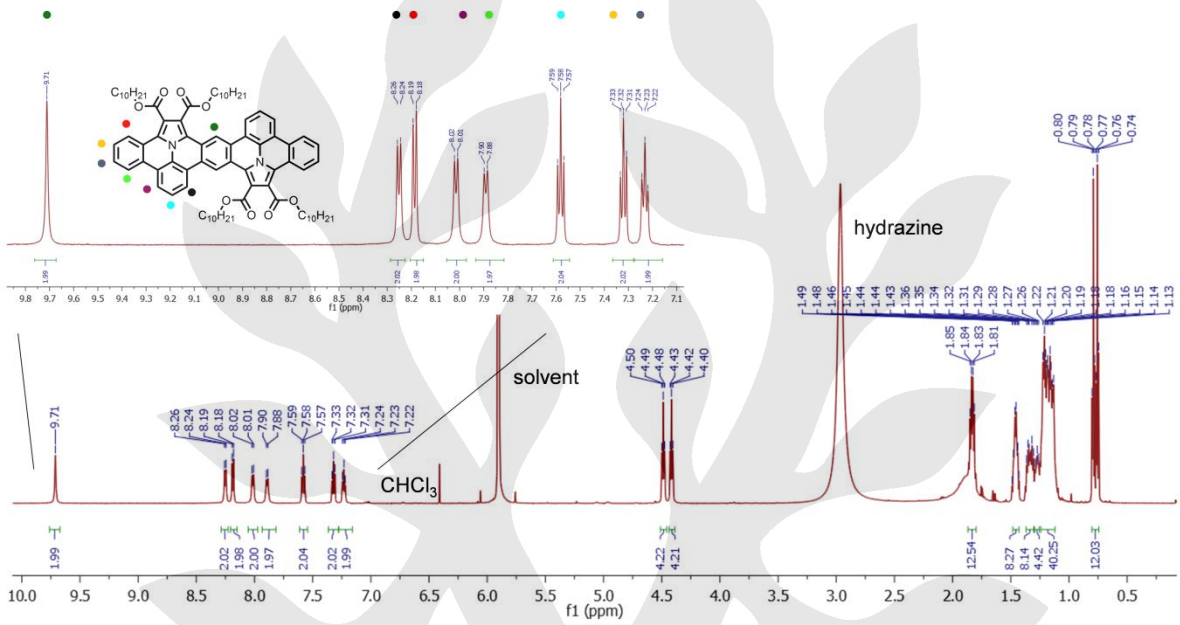

Figure S32. ^{1}H-NMR (600 MHz) spectrum of compound **DU-1** at 298 K in $C_2D_2Cl_4$.

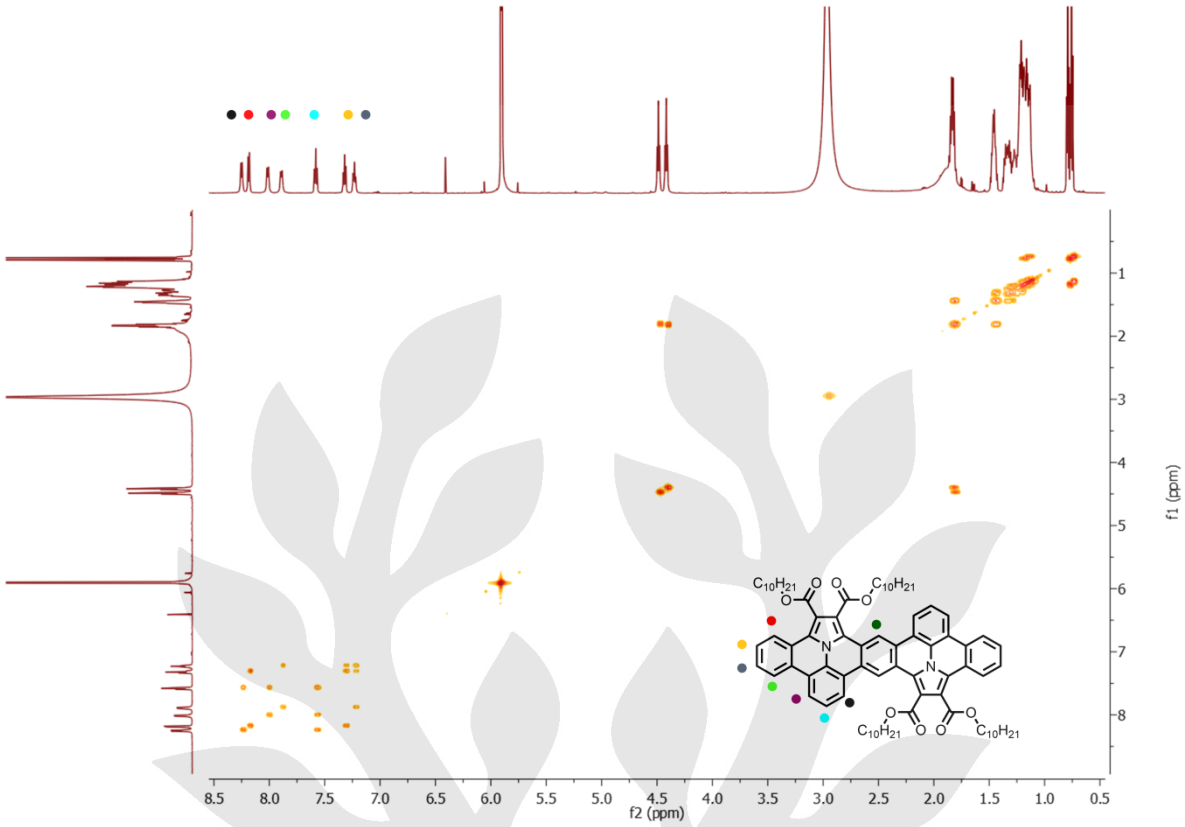

Figure S33. Correlation spectrum (COSY) of **DU-1** at 298 K in $C_2D_2Cl_4$.

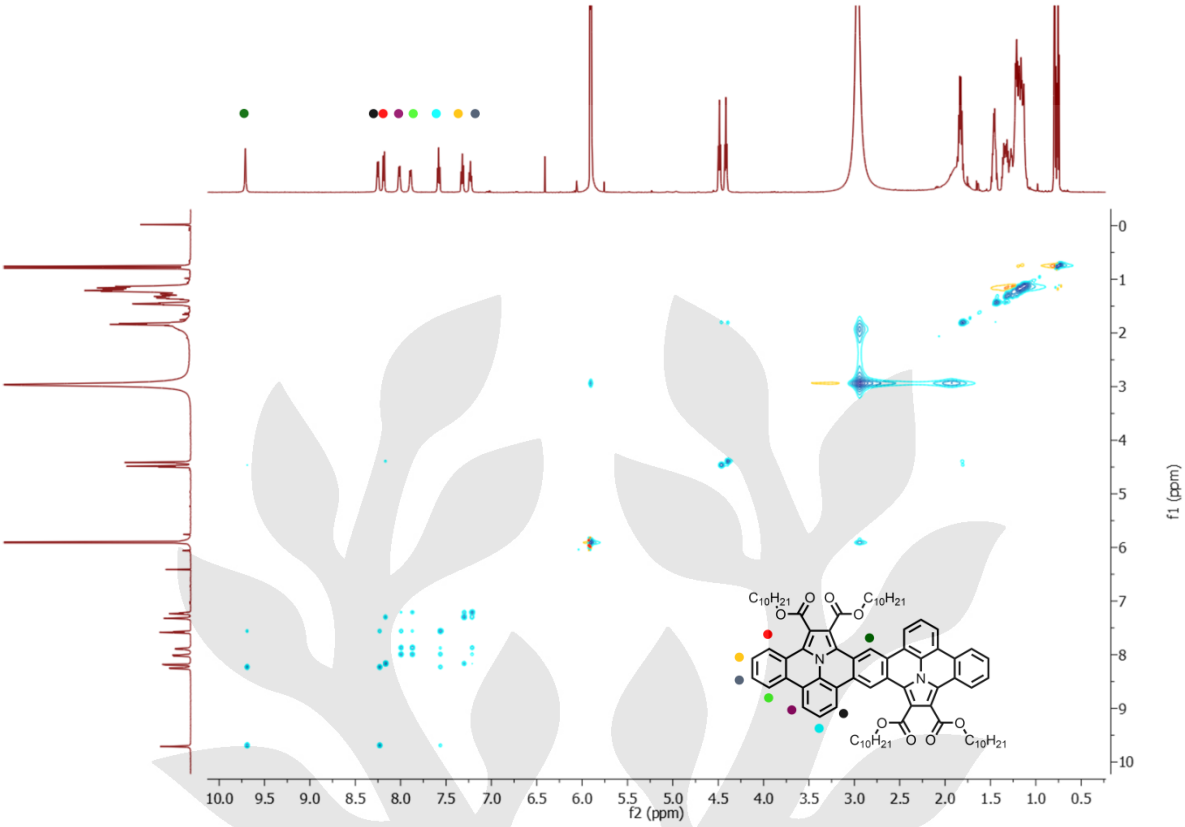

Figure S34. Nuclear Overhauser effect spectrum (NOESY) for **DU-1** at 298 K in $C_2D_2Cl_4$.

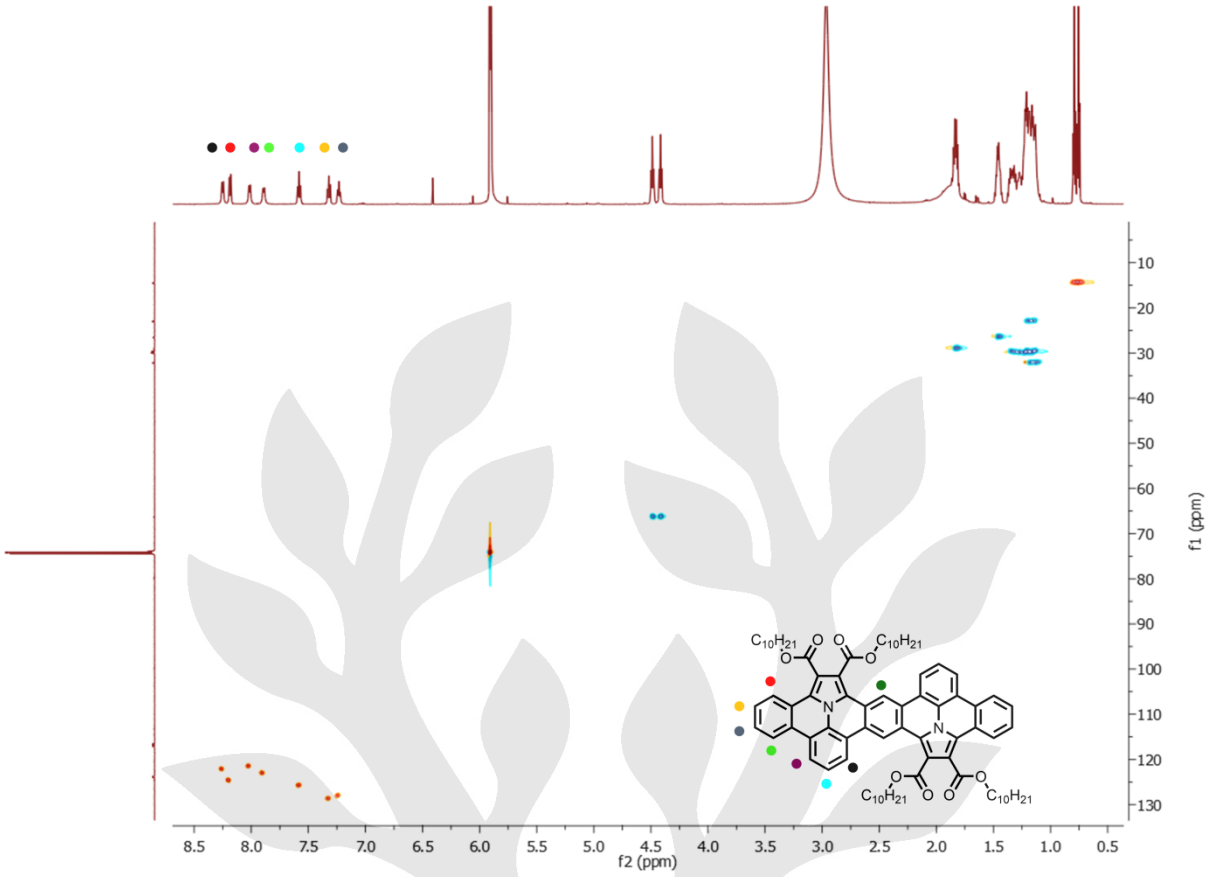

Figure S35. Heteronuclear single quantum coherence (HSQC) spectrum for **DU-1** at 298 K in $C_2D_2Cl_4$.

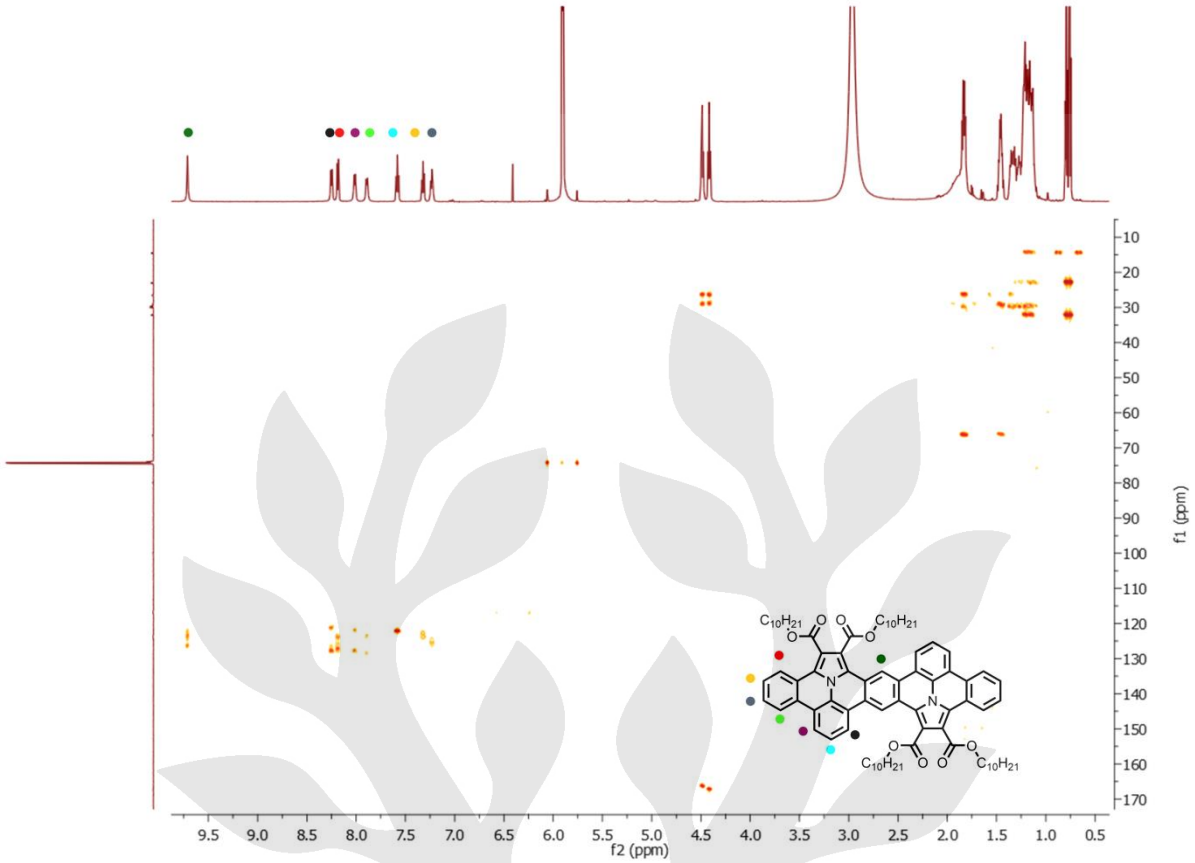

Figure S36. Heteronuclear multiple-bond correlation (HMBC) spectrum for **DU-1** at 298 K in $C_2D_2Cl_4$.

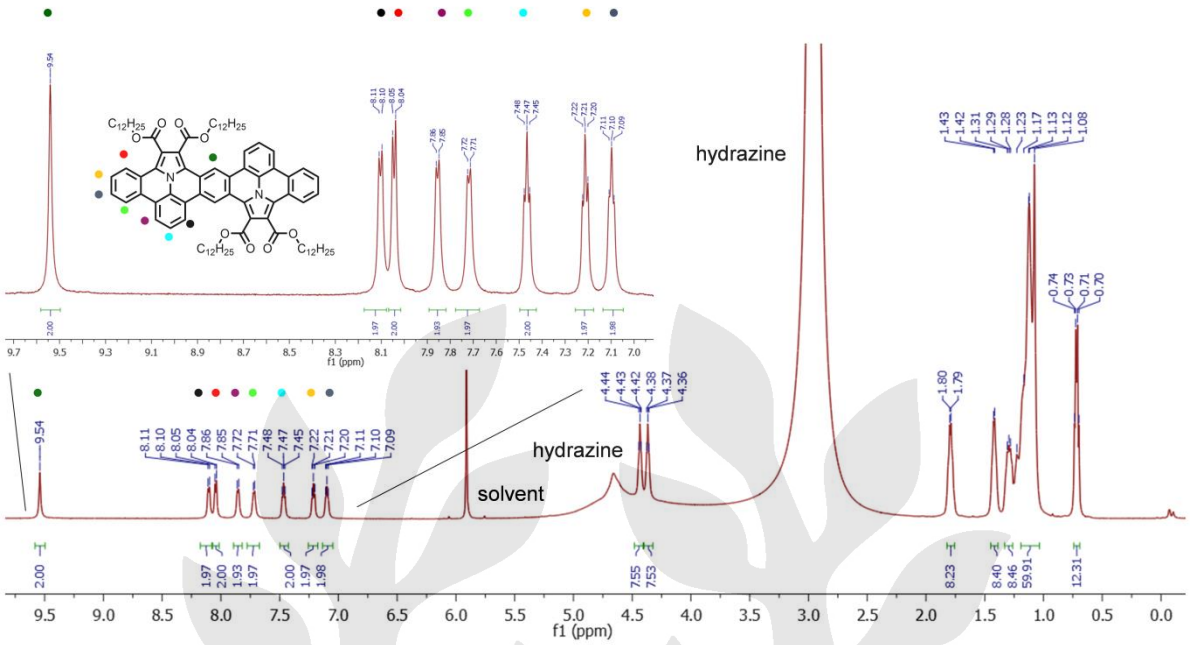

Figure S37. ^{1}H-NMR (600 MHz) spectrum of compound **DU-2** at 298 K in $C_2D_2Cl_4$.

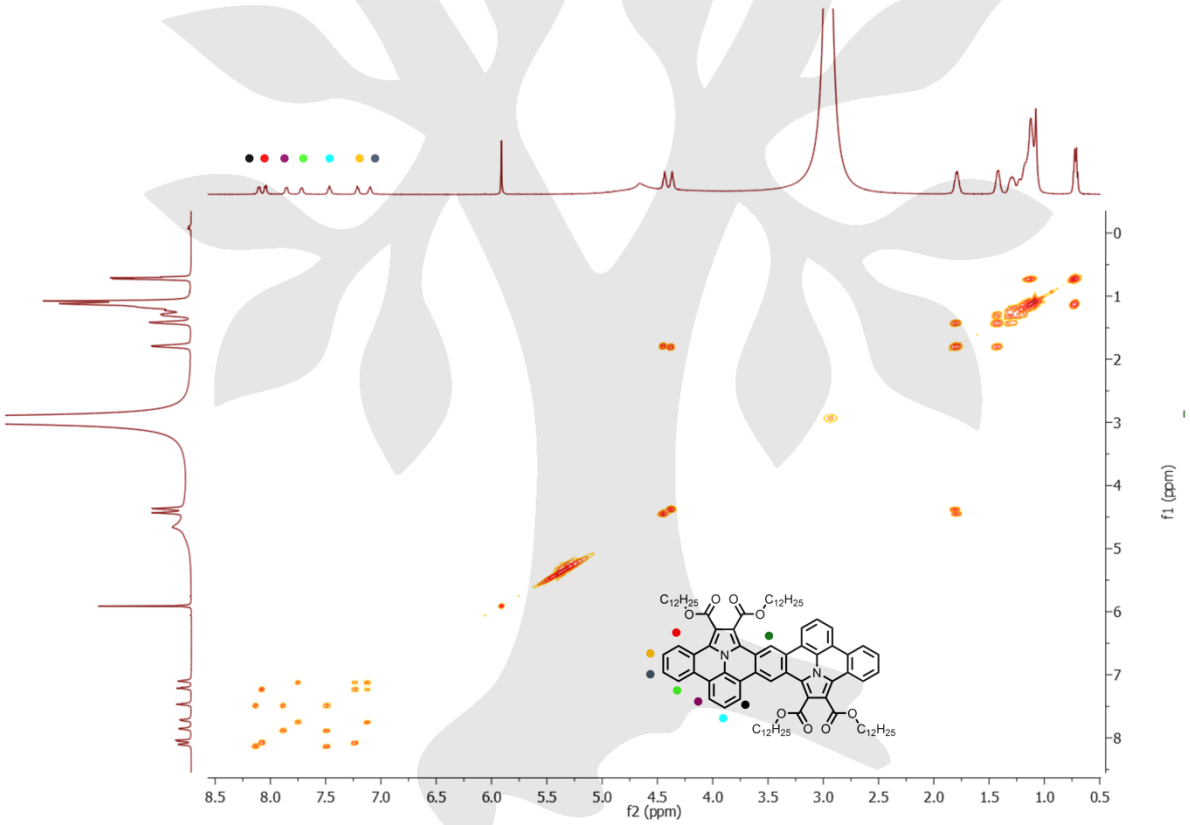

Figure S38. Correlation spectrum (COSY) of **DU-2** at 298 K in $C_2D_2Cl_4$.

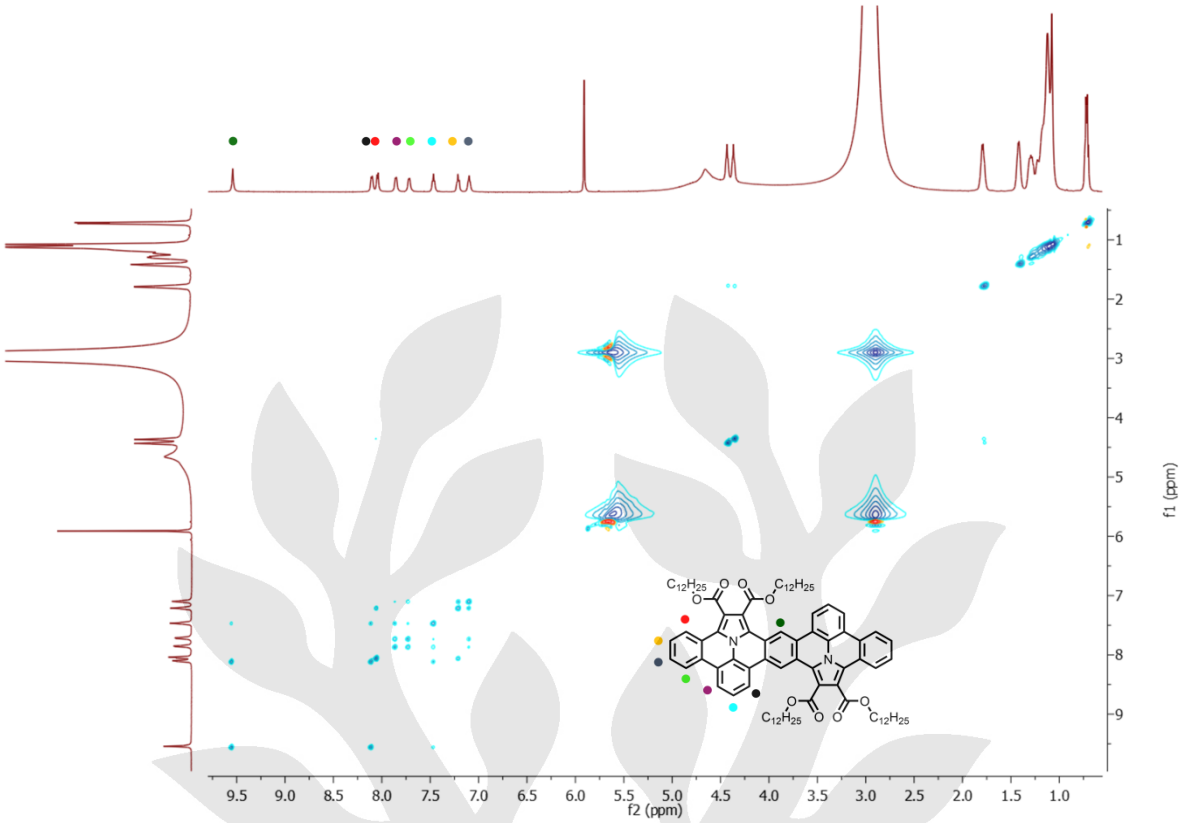

Figure S39. Nuclear Overhauser effect spectrum (NOESY) for **DU-2** at 298 K in $C_2D_2Cl_4$.

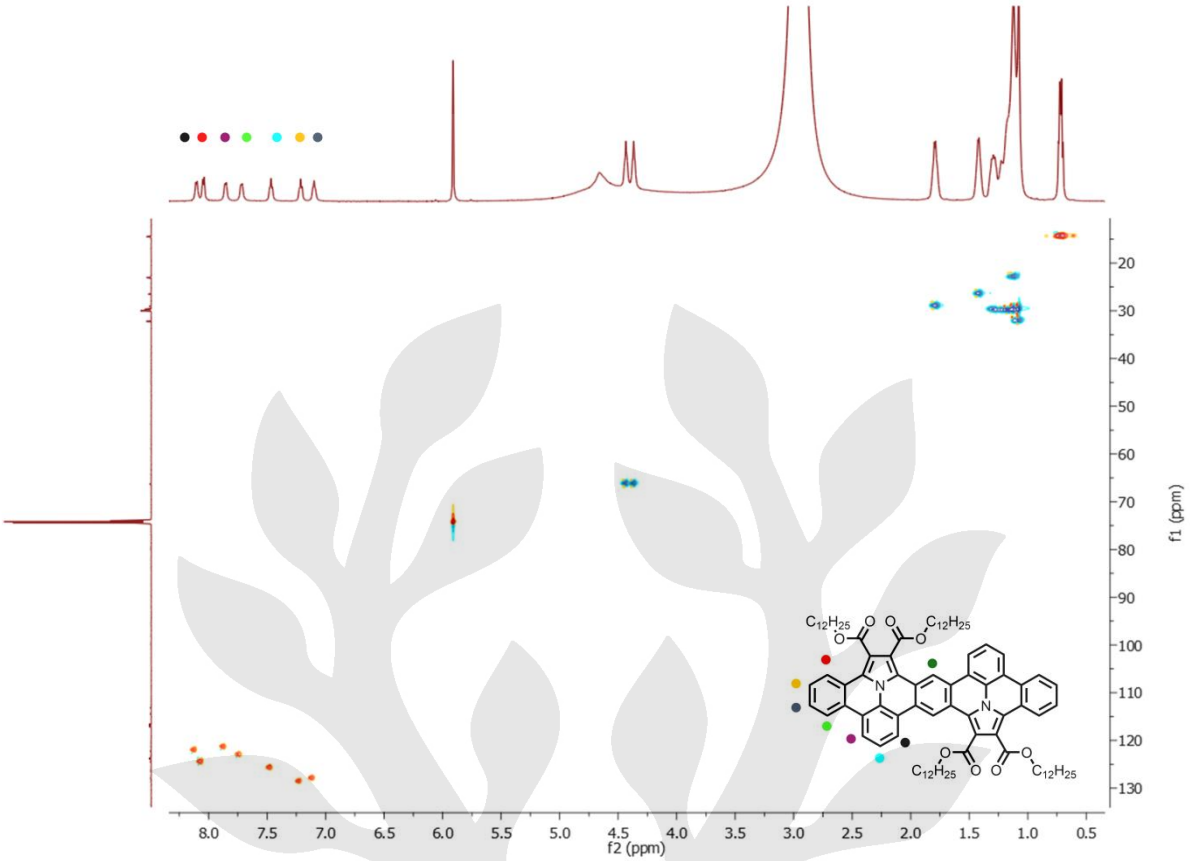

Figure S40. Heteronuclear single quantum coherence (HSQC) spectrum for **DU-2** at 298 K in $C_2D_2Cl_4$.

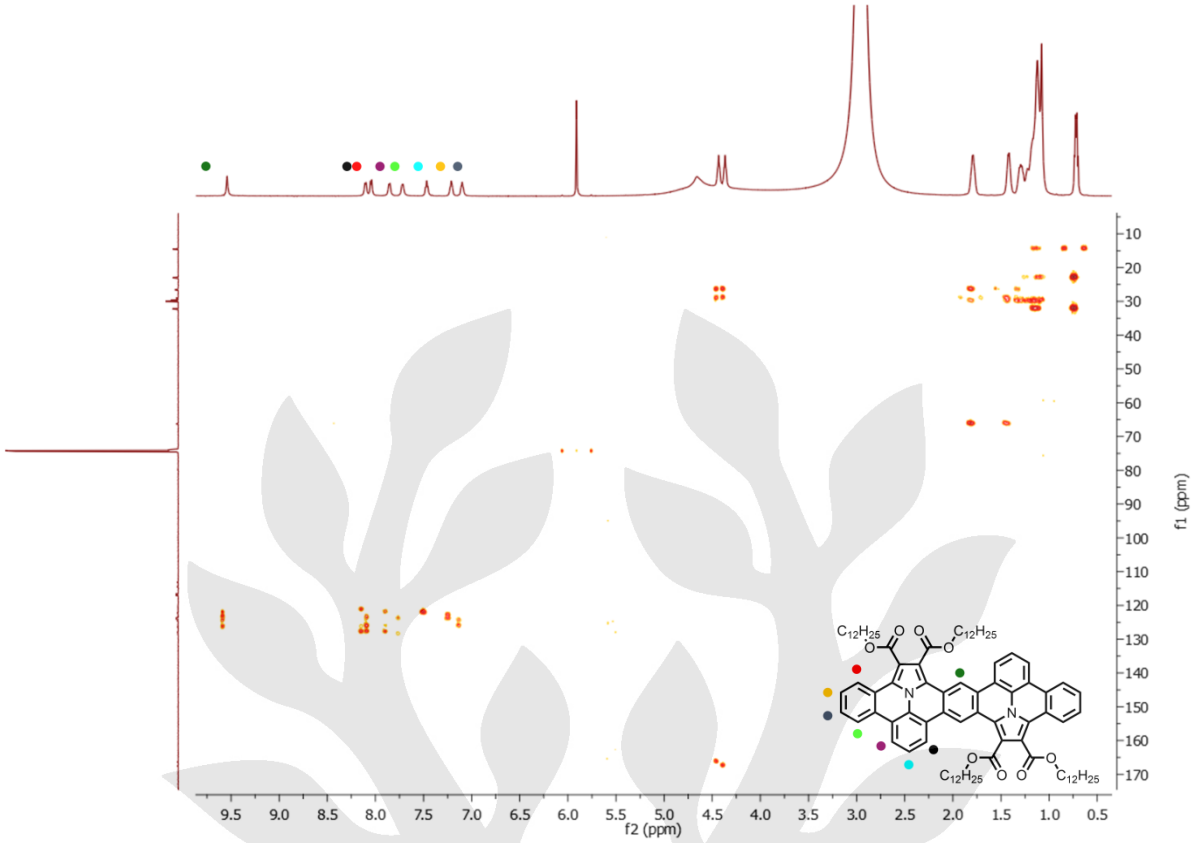

Figure S41. Heteronuclear multiple-bond correlation (HMBC) spectrum for **DU-2** at 298 K in $C_2D_2Cl_4$.

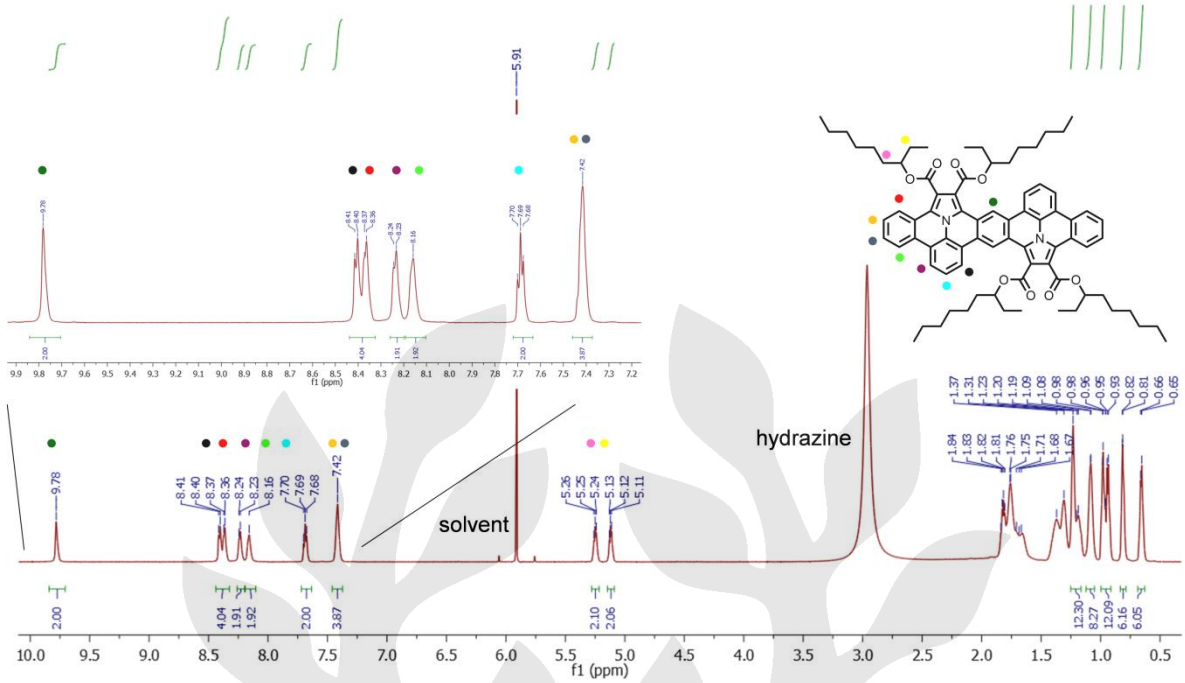

Figure S42. ^{1}H-NMR (600 MHz) spectrum of compound **DU-3** at 298 K in $C_2D_2Cl_4$.

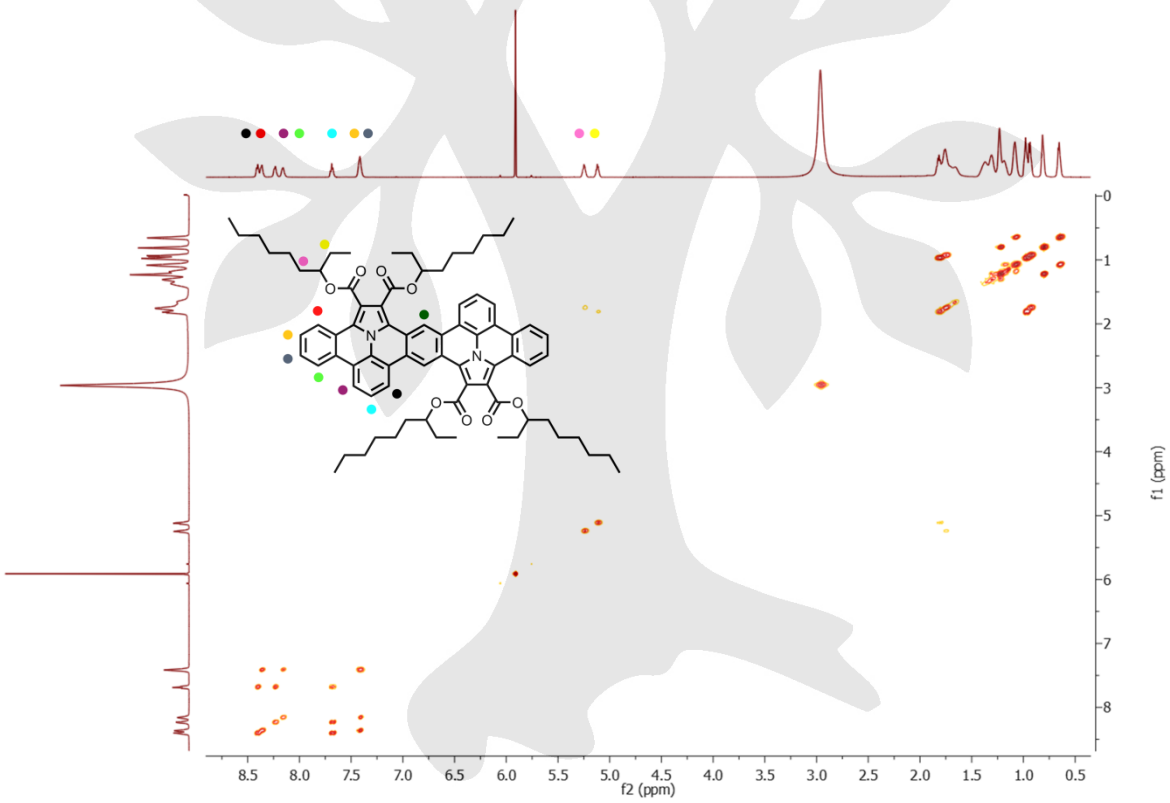

Figure S43. Correlation spectrum (COSY) of **DU-3** at 298 K in $C_2D_2Cl_4$.

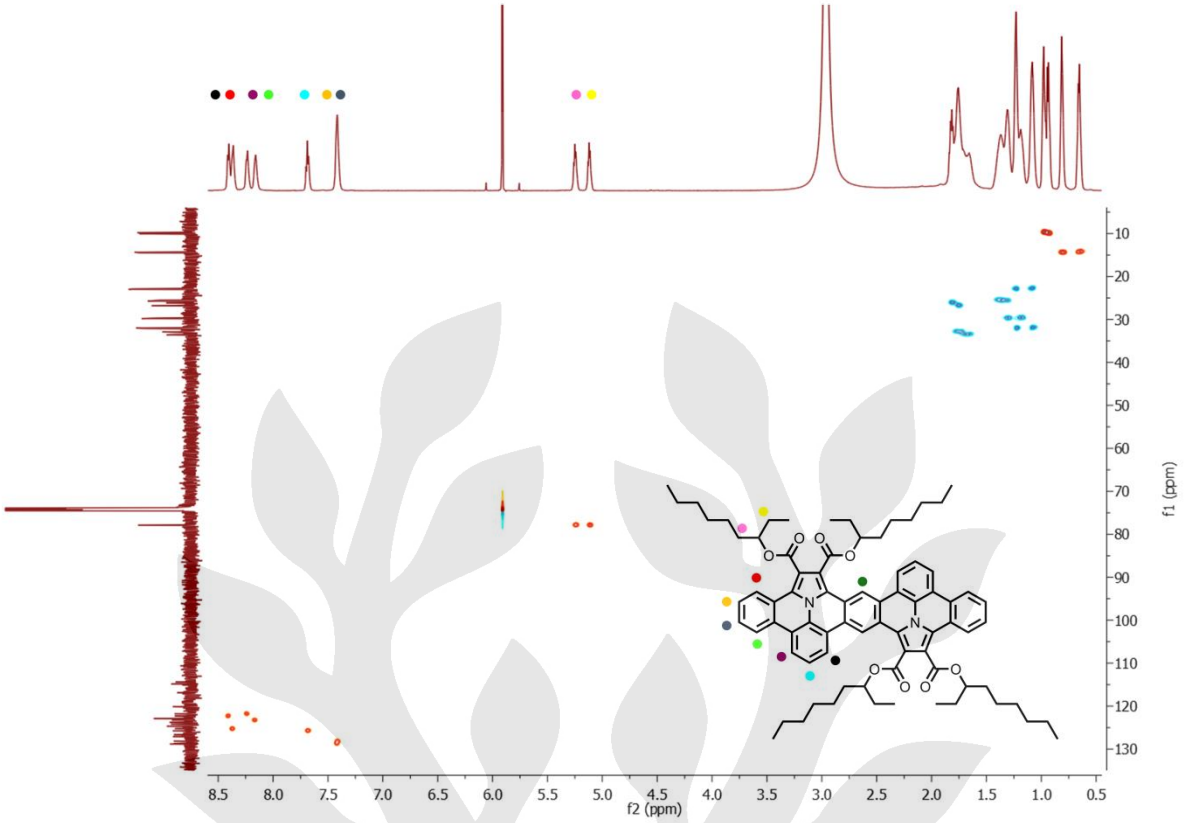

Figure S44. Heteronuclear single quantum coherence (HSQC) spectrum for **DU-3** at 298 K in $C_2D_2Cl_4$.

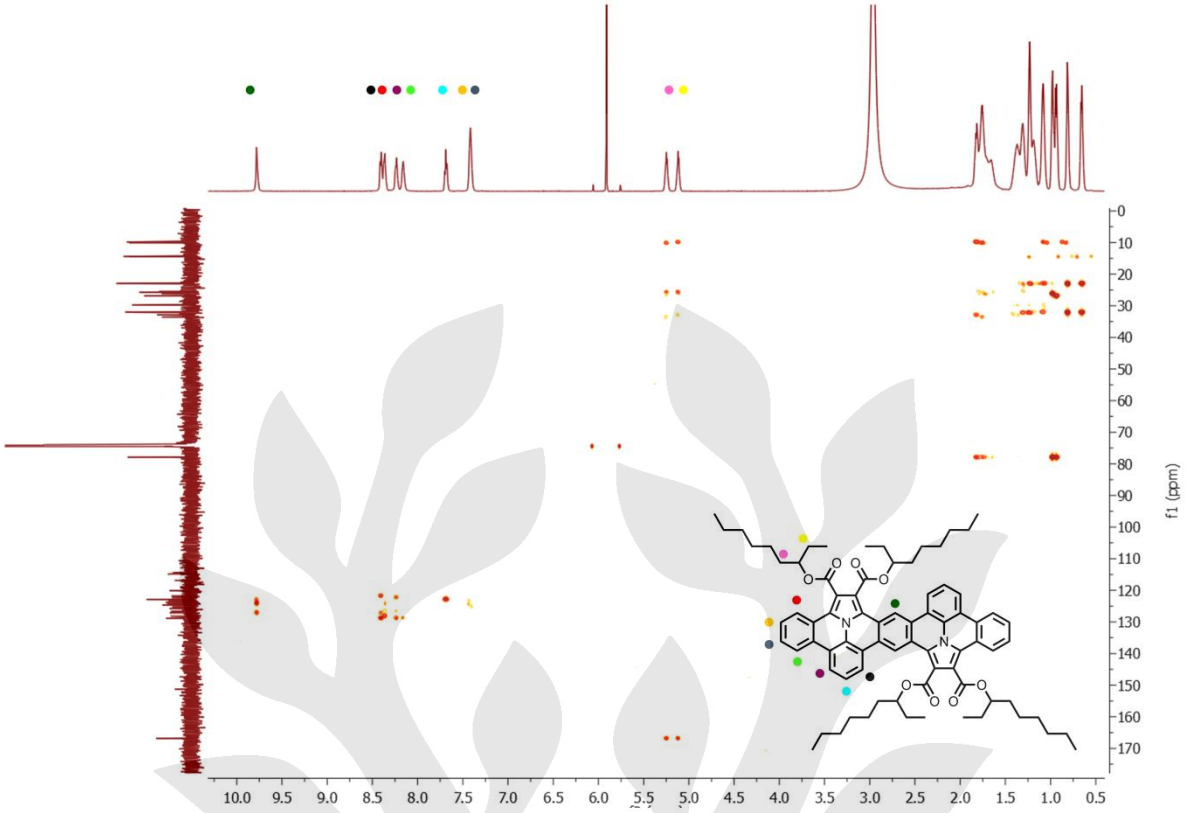

Figure S45. Heteronuclear multiple-bond correlation (HMBC) spectrum for **DU-3** at 298 K in $C_2D_2Cl_4$.

14) References

[1] M. J. C., W. H. Felix, F. R. H., *Advanced Materials* **1997**, *9*, 230-232.

[2] a) A. L. Appleton, S. M. Brombosz, S. Barlow, J. S. Sears, J.-L. Bredas, S. R. Marder, U. H. F. Bunz, *Nature Communications* **2010**, *1*, 91; b) C. M. Cardona, W. Li, A. E. Kaifer, D. Stockdale, G. C. Bazan, *Advanced Materials* **2011**, *23*, 2367-2371.

[3] A. Neudeck, A. Petr, L. Dunsch, *Synthetic Metals* **1999**, *107*, 143-158.

[4] M. J. Frisch, G. W. Trucks, H. B. Schlegel, G. E. Scuseria, M. A. Robb, J. R. Cheeseman, I. G. Scalmani, V. Barone, B. Mennucci, G. A. Petersson, H. Nakatsuji, M. Caricato, X. Li, H. P. Hratchian, A. F. Izmaylov, J. Bloino, G. Zheng, J. L. Sonnenberg, M. Hada, M. Ehara, K. Toyota, R. Fukuda, J. Hasegawa, M. Ishida, T. Nakajima, Y. Honda, O. Kitao, H. Nakai, T. Vreven, J. A. Jr. Montgomery, J. E. Peralta, F. Ogliaro, M. J. Bearpark, J. Heyd, E. N. Brothers, K. Kudin, V. N. Staroverov, R. Kobayashi, J. Normand, K. Raghavachari, A. P. Rendell, J. C. Burant, S. S. Iyengar, J. Tomasi, M. Cossi, N. Rega, N. J. Millam, M. Klene, J. E. Knox, J. B. Cross, V. Bakken, C. Adamo, J. Jaramillo, R. Gomperts, R. E. Stratmann, O. Yazyev, A. J. Austin, R. Cammi, C. Pomelli, J. W. Ochterski, R. L. Martin, K. Morokuma, V. G. Zakrzewski, G. A. Voth, P. Salvador, J. J. Dannenberg, S. Dapprich, A. D. Daniels, O. Farkas, J. B. Foresman, J. V. Ortiz, D. J. Cioslowski, D. Fox, Gaussian 09, Gaussian. Inc.: Wallingford, CT, **2009**.

[5] a) R. Berger, A. Giannakopoulos, P. Ravat, M. Wagner, D. Beljonne, X. Feng, K. Müllen, *Angewandte Chemie International Edition* **2014**, *53*, 10520-10524; b) R. Berger, A. Giannakopoulos, P. Ravat, M. Wagner, D. Beljonne, X. Feng, K. Müllen, *Angewandte Chemie* **2014**, *126*, 10688-10692.

[6] a) W. P. Forrest, J. G. Weis, J. M. John, J. C. Axtell, J. H. Simpson, T. M. Swager, R. R. Schrock, *Journal of the American Chemical Society* **2014**, *136*, 10910-10913; b) S. Marco, G. Luzia, S. Junji, S. A. Dieter, *European Journal of Organic Chemistry* **2015**, *2015*, 4519-4523.